Heliyon 10 (2024) e28244

Contents lists available at ScienceDirect

Heliyon

journal homepage: www.cell.com/heliyon

Research article

Integrative analysis of bulk and single-cell RNA-seq reveals the molecular characterization of the immune microenvironment and oxidative stress signature in melanoma

Yaling Li [a,b,c], Bin Jiang [a], Bancheng Chen [a], Yanfen Zou [a], Yan Wang [b], Qian Liu [b], Bing Song [b,c,**], Bo Yu [a,*]

[a] *Department of Dermatology, Institute of Dermatology, Peking University Shenzhen Hospital, Shenzhen Peking University-The Hong Kong University of Science and Technology Medical Center, Shenzhen, 518036, China*

[b] *Institute of Biomedical and Health Engineering, Shen Zhen Institutes of Advanced Technology, Chinese Academy of Science, Shenzhen, 518055, Guangdong, China*

[c] *Department of Dermatology, the First Hospital of China Medical University, Shenyang, 110001, Liaoning, China*

ARTICLE INFO

Keywords:
Melanoma
Immune microenvironment
Immune response
Oxidative stress
Prognosis
Tumor microenvironment

ABSTRACT

Background: The immune microenvironment and oxidative stress of melanoma show significant heterogeneity, which affects tumor growth, invasion and treatment response. Single-cell and bulk RNA-seq data were used to explore the heterogeneity of the immune microenvironment and oxidative stress of melanoma.

Methods: The R package Seurat facilitated the analysis of the single-cell dataset, while Harmony, another R package, was employed for batch effect correction. Cell types were classified using Uniform Manifold Approximation and Projection (UMAP). The Secreted Signaling algorithm from CellChatDB.human was applied to elucidate cell-to-cell communication patterns within the single-cell data. Consensus clustering analysis for the skin cutaneous melanoma (SKCM) samples was executed with the R package ConsensusClusterPlus. To quantify immune infiltrating cells, we utilized CIBERSORT, ESTIMATE, and TIMERxCell algorithms provided by the R package Immuno-Oncology Biological Research (IOBR). Single nucleotide variant (SNV) analysis was conducted using Maftools, an R package specifically designed for this purpose. Subsequently, the expression levels of *PXDN* and *PAPSS2* genes were assessed in melanoma tissues compared to adjacent normal tissues. Furthermore, in vitro experiments were conducted to evaluate the proliferation and reactive oxygen species expression in melanoma cells following transfection with siRNA targeting *PXDN* and *PAPSS2*.

Results: Malignant tumor cell populations were reclassified based on a comprehensive single-cell dataset analysis, which yielded six distinct tumor subsets. The specific marker genes identified for these subgroups were then used to interrogate the Cancer Genome Atlas Skin Cutaneous Melanoma (TCGA-SKCM) cohort, derived from bulk RNA sequencing data, resulting in the delineation of two immune molecular subtypes. Notably, patients within the cluster2 (C2) subtype exhibited a significantly more favorable prognosis compared to those in the cluster1 (C1) subtype. An alignment of immune characteristics was observed between the C2 subtype and unique immune

* Corresponding author.

** Corresponding author. Institute of Biomedical and Health Engineering, Shen Zhen Institutes of Advanced Technology, Chinese Academy of Science, Shenzhen, 518055, Guangdong, China.

E-mail addresses: bing.song@siat.ac.cn (B. Song), yubomd@163.com (B. Yu).

https://doi.org/10.1016/j.heliyon.2024.e28244
Received 30 September 2023; Received in revised form 11 March 2024; Accepted 14 March 2024
Available online 15 March 2024

functional tumor cell subsets. Genes differentially expressed across these subtypes were subsequently leveraged to construct a predictive risk model. In vitro investigations further revealed elevated expression levels of *PXDN* and *PAPSS2* in melanoma tissue samples. Functional assays indicated that modulation of *PXDN* and *PAPSS2* expression could influence the production of reactive oxygen species (ROS) and the proliferative capacity of melanoma cells.
Conclusion: The constructed six-gene signature can be used as an immune response and an oxidative stress marker to guide the clinical diagnosis and treatment of melanoma.

1. Introduction

Among the different malignancies, melanoma is one of the most common kinds. It is a highly malignant tumor originating from neural crest melanocytes and is characterized by early metastasis, strong invasiveness, and poor prognosis. Over the past 30 years, melanoma's incidence and mortality rate have continued to increase. This is indicated by the annual increase rate of 3%–5%. The incidence of skin melanoma is 91.2%, eye melanoma is 5.3%, mucosal melanoma is 1.3%, and melanoma in other parts of the body is 2.2% [1]. Early-stage melanoma can be treated with surgery and a good prognosis; however, the survival rates of regional and distant metastatic melanoma patients have reduced to 63% and 20%, respectively [2]. Immunoassay block therapy and molecular targeted therapy, including cytotoxic T-lymphocyte–associated antigen 4 (CTLA-4) inhibitors, programmed cell death ligand 1 (PD-1/PDL1) inhibitors, and v-raf murine sarcoma viral oncogene homolog B1 (BRAF) inhibitors, are the preferred treatments for advanced melanoma [3,4]. However, melanoma is highly heterogeneous, so the response to immunotherapy varies. Hence, investigating the unique malignant cell subsets of melanoma immunity for individualized treatment is crucial.

Previous studies on molecular expression patterns in organisms usually used the average expression level of multiple cells in a sample. However, the expression of various biomolecules varies greatly even across different cells within the same sample. Recent developments in single-cell sequencing technology have made the accurate quantification of biological data in a single cell possible [5,6]. The cells that perform a vital function in tumorigenesis and progression are usually lesser in number. Single-cell sequencing data can identify these rare cell types. Recent studies have explored the spatial landscape of melanoma immune editing at a single-cell resolution [7], providing a theoretical basis for our analysis.

This study utilized single-cell dataset analysis for characterizing the heterogeneous nature of the immune cells that infiltrate the

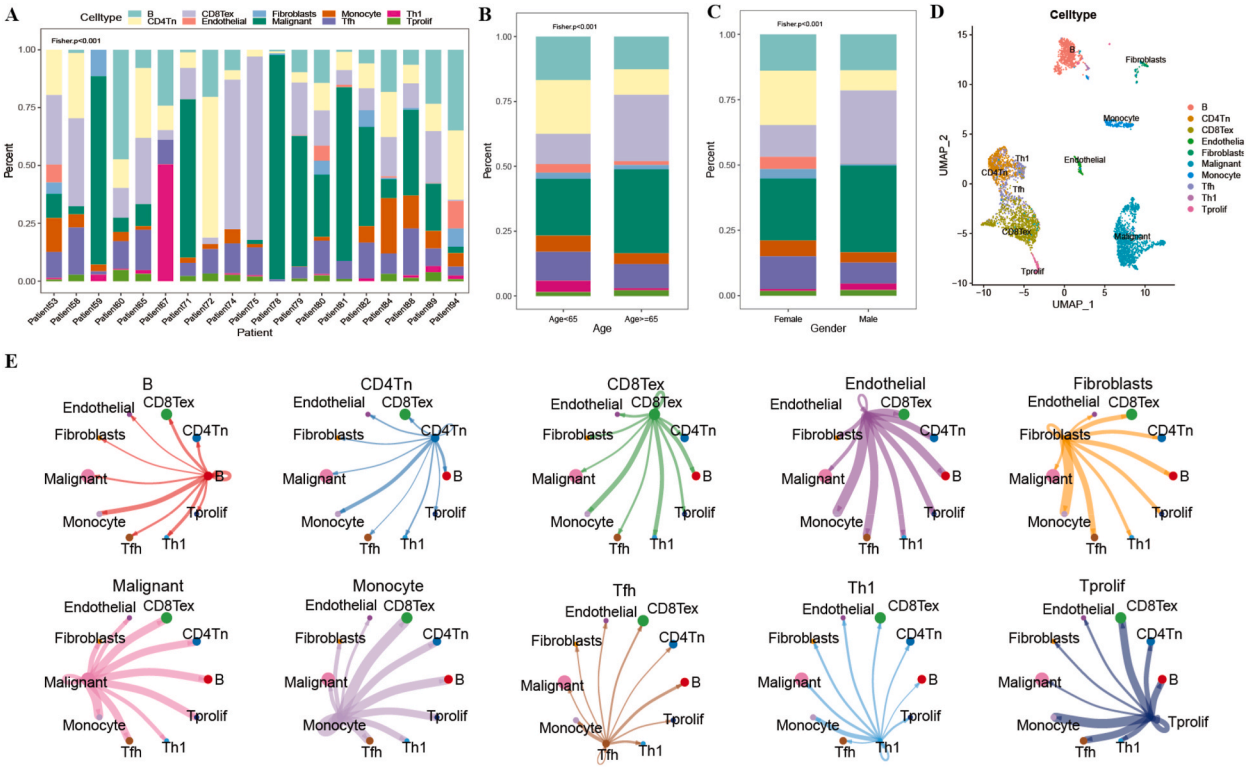

Fig. 1. Heterogeneity of tumor single cells. A-C. In the single-cell dataset, patients/age/sex were taken as the grouping information, and the distribution differences of cell types in each group were counted; D. The UMAP of cell subset distribution; E. Cell communication weight map of each cell subpopulation and other subpopulations. The size of the dots and the thickness of the lines represent the communication intensity.

tumor cells in melanoma patients. It also identified a subset of tumor cells with specific immune functions. The immunotyping of TCGA_SKCM bulk RNA dataset as per the specific marker genes in this subpopulation was performed. The relationship between melanoma prognosis and the expression perturbation of this gene set was explored from multiple perspectives. This was done to reveal the potential function of the immune functional cell population in course of tumor treatment. The genes with differential expression among the subtypes were utilized to fabricate a prognostic risk score model. Additionally, the risk score model's relationship with the cancer immune microenvironment, immune function, genomic variation, and chemotherapy resistance was explored.

2. Results

2.1. Recognition of specific immune tumor cell subsets

2.1.1. Tumor single-cell landscape

Analyzing single-cell datasets can help explore the tumor immune microenvironment and discover new functional cell subsets. Initially, the clinical information and cell types of patients in the selected single-cell dataset were statistically analyzed and visualized (Table S1). The distribution of cell types among each patient differed, indicating that the tumor microenvironment had obvious individual differences (Fig. 1A). There were also significant differences in the cell-type distribution based on age (Fig. 1B) and gender (Fig. 1C).

Through the constructed Seurat object, the UMAP dimension reduction was utilized for identifying the cell-type distribution (Fig. 1D). The malignant cells were clustered together, indicating strong differences in the malignant cells and other cells at the transcriptome level. Based on the cell types and expression information of single cells, the R package CellChat was used for characterizing the communication between the cell subsets. The CD8 cells, CD4 cells, B cells, and other cells communicated closely (Fig. 1E).

2.1.2. Subdivision of malignant cells subsets

The malignant cells were screened, and the number of subsets in the existing literature was referenced for debugging. Finally, the

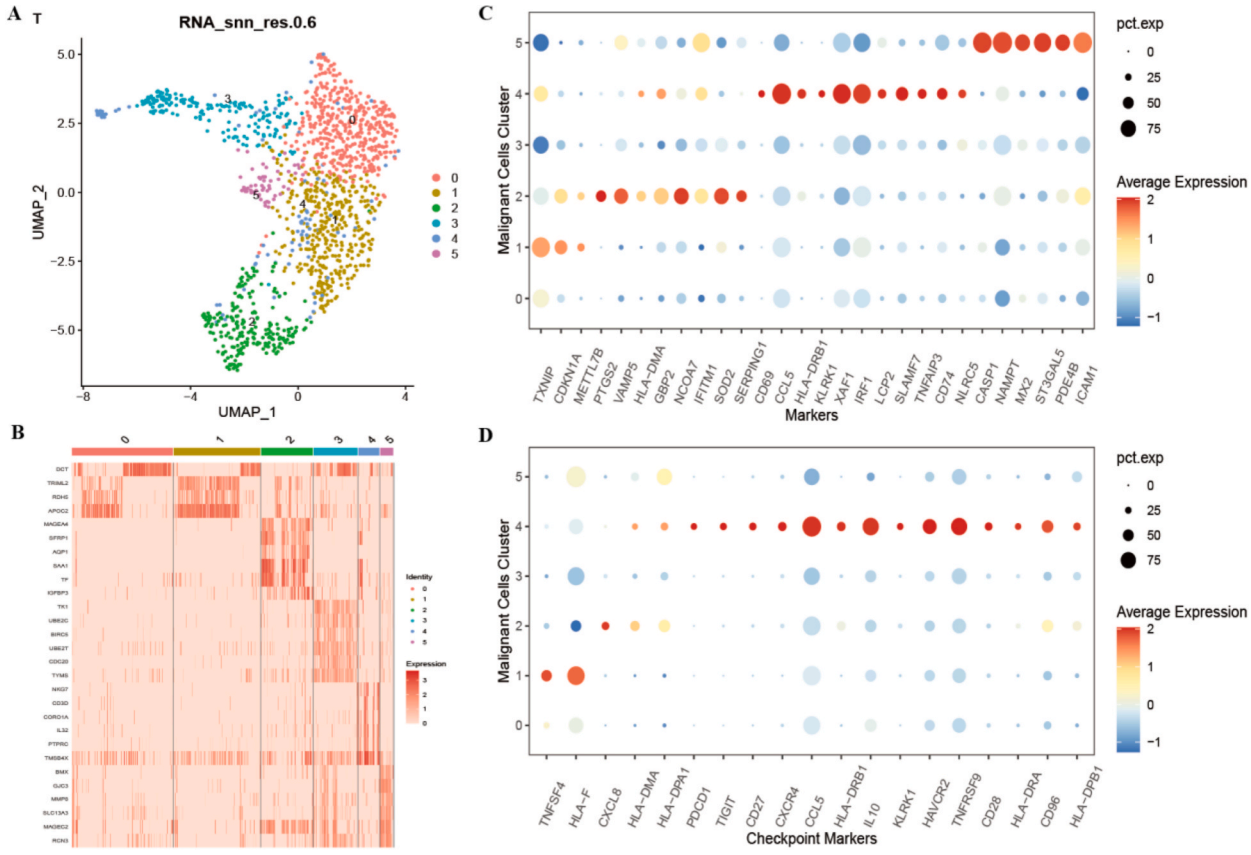

Fig. 2. Malignant cell subsets and their expression characteristics. A. The UMAP of the results of regrouping of malignant cells; B. TOP6 marker expression heatmap of malignant cell subsets; C-D. Bubble plots of interferon response factors and immune checkpoint genes specifically expressed in the malignant cell subsets. The size of the dots represents the number of cells expressed in the subpopulation, and the color represents the average expression level. (For interpretation of the references to color in this figure legend, the reader is referred to the Web version of this article.)

malignant cell subsets were identified with a 0.6 resolution. Fig. 2A shows the cluster results with the UMAP dimensionality reduction. The subgroup marker genes were identified based on the aforementioned clustering results, and afterward, the most specific TOP6 (logFC value) genes of each subgroup were screened to draw a heatmap (Fig. 2B). The gene expression bubble map was drawn for the marker genes in the subsets, and the expression of the interferon response factors and immune checkpoints in the six cell subsets was further explored. The immune interferon response factors were highly expressed in TC4 and TC5, while the immunosuppressive factors were highly expressed in TC4 (Fig. 2C–D).

2.2. Functional identification of malignant cell subsets and recognition of the special immune subsets

To identify which of the six subsets had a special immune function, the GSEA gene sets enrichment analysis was performed on the marker genes of all subsets based on the KEGG pathway. An NES heatmap was drawn for the pathways enriched in all six subsets to show the differences in the KEGG pathway enrichment (Fig. 3A). The top five pathways significantly enriched in TC4 were screened for demonstration. The pathways ANTIGEN_PROCESSING_AND_PRESENTATION and CHEMOKINE_SIGNALING of TC4 were significantly enriched (Fig. 3B). Subsequently, a gene ontology (GO) enrichment analysis was conducted on the marker genes of all the subsets, and the top 10 pathways with significant enrichment were selected. The marker genes of TC4 were significantly enriched in the pathways related to immune response (Fig. 3C). Simultaneously, the GSEA gene sets (Hallmark) enrichment analysis was conducted according to the logFC size order. The results indicated that the INTERFERON_GAMMA_RESPONSE pathway in the TC4 enrichment pathway was correlated to cancer immunity, and the enrichment results were examined (Fig. 3D). These analyses indicated that TC4 had a special immune function, and the expression distribution of its top six marker genes in malignant subgroups was examined (Fig. 3E).

2.3. Recognition and characterization of the specific immune subtypes

2.3.1. Potential of the specific immune subsets to distinguish between patients

A threshold of avg_log2FC > 1 was used to screen 62 marker genes specific to the TC4 subgroup (Table S2), and cluster analysis helped identify the immune molecular subtypes as per the expression of the aforementioned genes in TCGA cohort. In cases of partition around medoids (PAM) clustering algorithm and Spearman's distance, the clustering effect was the best: bestK = 2 (Fig. 4A–D). The

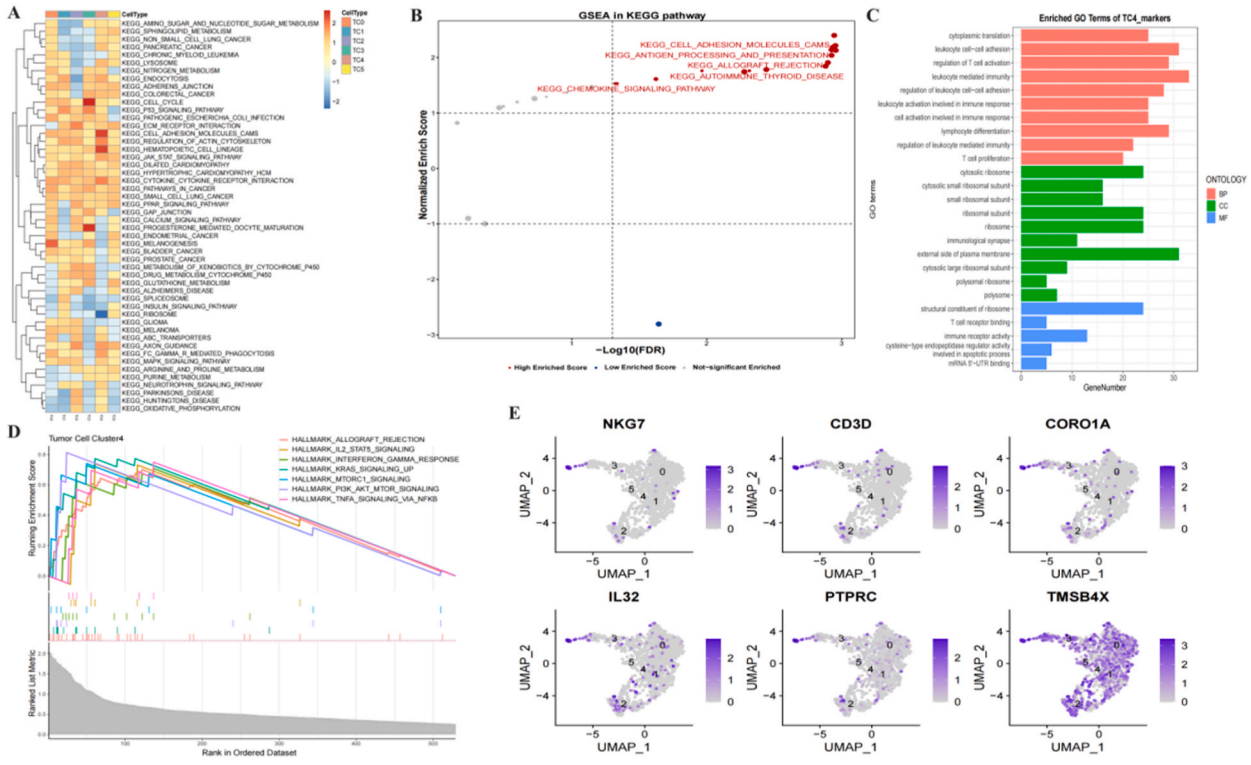

Fig. 3. Communication between tumor subsets and other cells. A. NES heatmap of significantly enriched pathways in the GSEA analysis of subsets. The larger the NES, the more significantly enriched the NES in this pathway; B. The KEGG GSEA pathway of the TC4 subgroup was significantly enriched. The size of dots represents GeneRadio, red represents NES>1, and blue represents NES < −1; C. Hallmark GSEA enrichment results of the TC4 subgroup; D. Histogram of the significantly enriched GO Terms for the TC0 subgroup, with the horizontal coordinate representing the number of enriched marker genes; E. The UMAP of expression distribution of the TOP 6 marker genes of the TC4 subgroup. (For interpretation of the references to color in this figure legend, the reader is referred to the Web version of this article.)

cumulative distribution function (CDF) of the consistent clustering showed the CDF when K assumed various values (Fig. 4E). The variation of the area under the CDF curve, wherein K was relative to K-1, was shown (Fig. 4F). The two identified independent molecular subtypes associated with the immune system varied significantly in their survival rates. These were illustrated in a figure wherein the considerably better prognosis of the C2 subtype compared to the C1 subtype was depicted (Fig. 4G–J). Finally, the PCA and the t-distributed stochastic neighbor embedding (t-SNE) algorithm were used respectively to reduce the data dimensionality, and a two-dimensional (2D) scatter plot was drawn to authenticate the reliability of the clustering results. The two subtypes were divided, indicating that the abovementioned clustering results were good (Fig. 4K-L).

2.3.2. *Differences in the expression and clinical characteristics of the immune subtypes*

Based on the typing results, the differential expression analysis of C1 and C2 was utilized to detect the genes with subtype differences, and a volcano map was drawn. The specific marker genes of the TC4 subgroup were annotated in the volcano map. A total of 412 significantly-different genes were obtained (Table S3), wherein most genes depicted increased expression in the C2 subtype (Fig. 5A). The intersection of the differentially-expressed genes and the specific marker genes of TC4 was noted, and the expression heatmap of the intersection genes was drawn (Fig. 5B). Finally, to identify functional differences in the immune subtypes, an enrichment analysis of the GO and KEGG pathways based on the differentially-expressed genes was conducted, and bubble maps of the 10 most significant pathways were drawn. The analyses highlighted the increased enrichment of the differential genes in the immune T-cell and major histocompatibility (MHC) molecular-related pathways (Fig. 5C–F). This proved that there were differences in the immune function among the subtypes. The C2 subtype had a stronger immune function, which was conducive to the SKCM prognosis.

2.3.3. *Differences in the immune microenvironment of the immune subtypes*

Functional differences in the immune subtypes were investigated. The enrichment scores of 50 Hallmark pathways were estimated

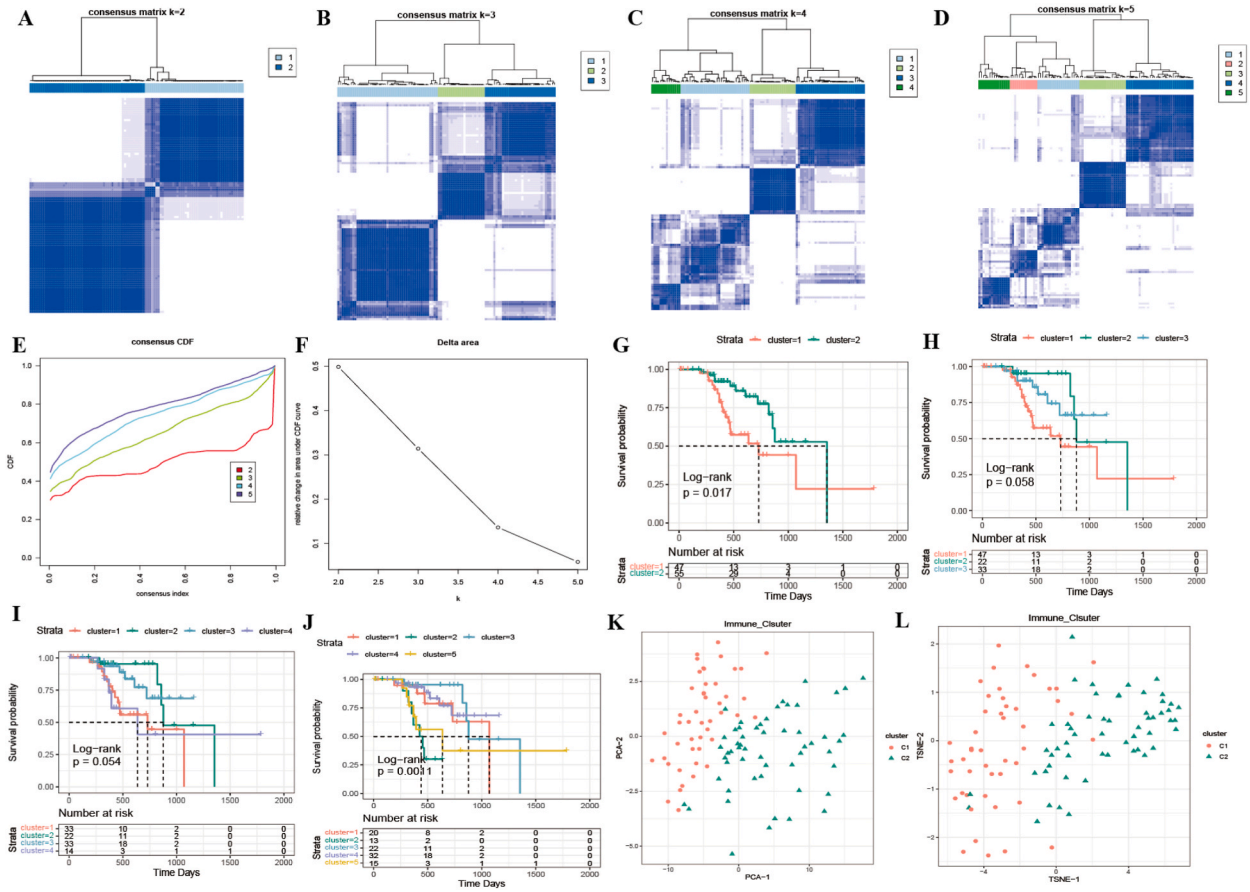

Fig. 4. Recognition results of TCGA immune subtypes. A-D. The clustering results when the number of classifications was k = 2, k = 3, k = 4, and k = 5, respectively; E. The CDF curve distribution of the consistent clustering; F. Distribution of the area under the CDF curve of the consistent clustering; G-J. The survival curve when the number of categories was k = 2, k = 3, k = 4, k = 5, respectively; K. The PCA dimensionality reduction algorithm showed the scatter plot of the typing results, with red representing C1 and green representing C2; L. The T-SNE algorithm shows the scatter plot of the typing results, with red representing C1 and green representing C2. (For interpretation of the references to color in this figure legend, the reader is referred to the Web version of this article.)

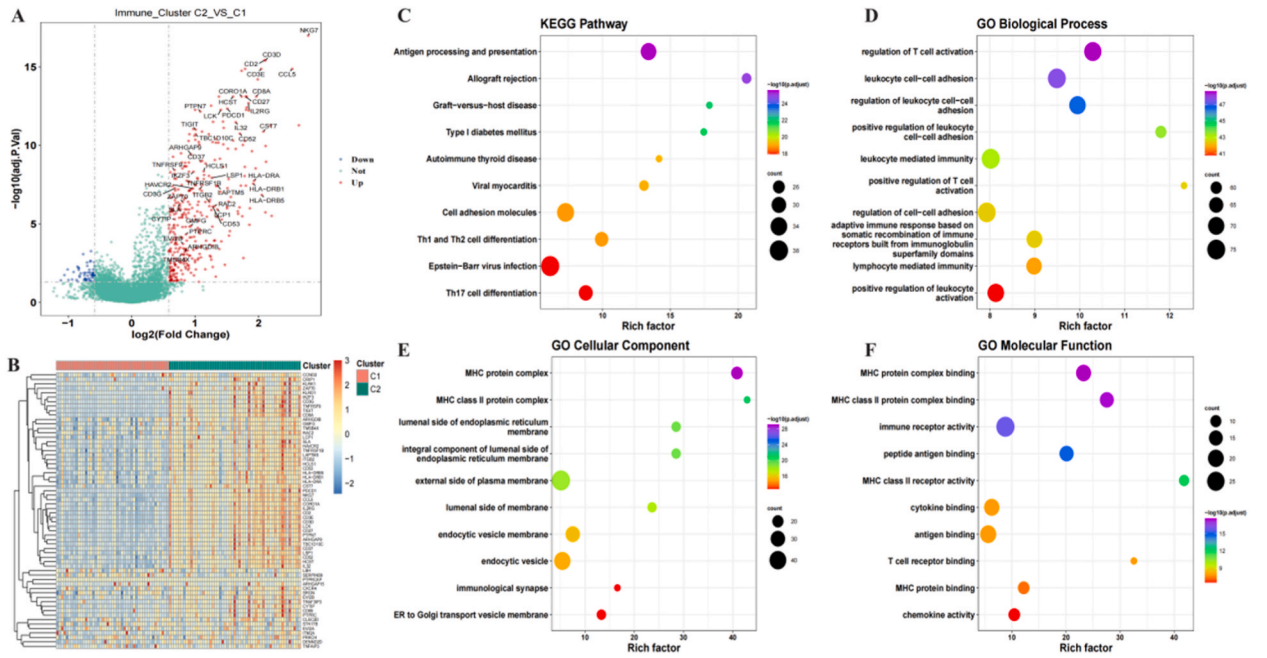

Fig. 5. Differences in the expression and clinical characteristics of TCGA immune subtypes. A. Volcano map of differentially-expressed genes where red represents high expression, blue represents low expression, and green represents insignificant expression difference; B. Heatmap of the marker gene expression of TC4 in the immune subtypes; C–F: Bubble diagram of the GO and KEGG enrichment analysis of the differentially-expressed genes. The size of the dots represents the number of marker genes enriched, and the color represents the significance of enrichment. (For interpretation of the references to color in this figure legend, the reader is referred to the Web version of this article.)

as per the melanoma-related gene expression data. These were then combined with other clinical features to create a heatmap to show enrichment differences between the two subtypes. The IL2_STAT, IL6_STAT related pathways, and interferon response-related pathways were significantly enriched in C2 (Fig. 6A). The enrichment scores of the immune function gene sets were calculated, and the results showed that the C2 subtype of most immune characteristic gene sets had higher enrichment scores (Fig. 6B). Box plots were used to view and compare the expression differences of the immune checkpoint inhibitors across the immune subtypes, yielding results similar to that of the functional enrichment analysis (Fig. 6C). The analyses indicated the considerably enhanced expression of C2 compared to C1.

Additionally, immune cells and stromal cells are the two main types of non-tumor components in the tumor microenvironment. These have been proposed to be valuable for tumor diagnosis and prognostic assessment. We calculated the proportion of the immune infiltrating cells in each sample using four common methods. We then displayed the differences in the immune infiltration of the immune subtypes through box plots. The results are shown in Fig. 7A: CIBERSORT. The calculated infiltration ratios of 22 immune cell types between the subtypes were different. Significant differences in the infiltration ratios of 12 cell types were observed. The infiltration ratio of T_cell_CD8 in C2 was significantly higher than that in C1. Fig. 7B shows the differences in the infiltration ratios of the six immune cell categories calculated by the TIMER algorithm. Similarly, the infiltration ratio of the T_cell_CD8 in C2 was significantly higher than that in C1. Panel C is a box plot of the difference between the four ESTIMATE scores across the subtypes. The C2 subtype had a significantly higher stromal score, immune score, and ESTIMATE score than C1, while the tumor purity was lower than that of C1 (Fig. 7C).

2.3.4. Genomic mutation differences in the immune subtypes

To study the mutation differences of the immune subtypes at the genome level, we used the SNV data from TCGA_SKCM dataset to draw a waterfall diagram. This diagram was utilized to show the mutation distribution of the top 20 genes with mutation frequency in the dataset in the sample. Titin (TTN) had the highest mutation frequency (Fig. 8A). The TMB differences among subtypes were analyzed by calculating the TMB of the samples. Enhanced TMB values in the C2 group were observed (Fig. 8B). The genomic mutation waterfall between subtypes was shown, wherein the mutation frequency of TTN and MUC16 in C2 was more enhanced than in C1. However, the mutation frequency of BRAF in C1 was depicted to be considerably increased than that of C2 (Fig. 8C–D), which revealed that the BRAF mutation may be detrimental to the SKCM prognosis.

2.4. Construction of the prognostic models based on differential genes of the specific immune subtypes

2.4.1. Prognosis signature identification of melanoma

The genes depicting differential expression in the subtypes were filtered out using univariate cox analysis ($P < 0.05$), and 30 genes

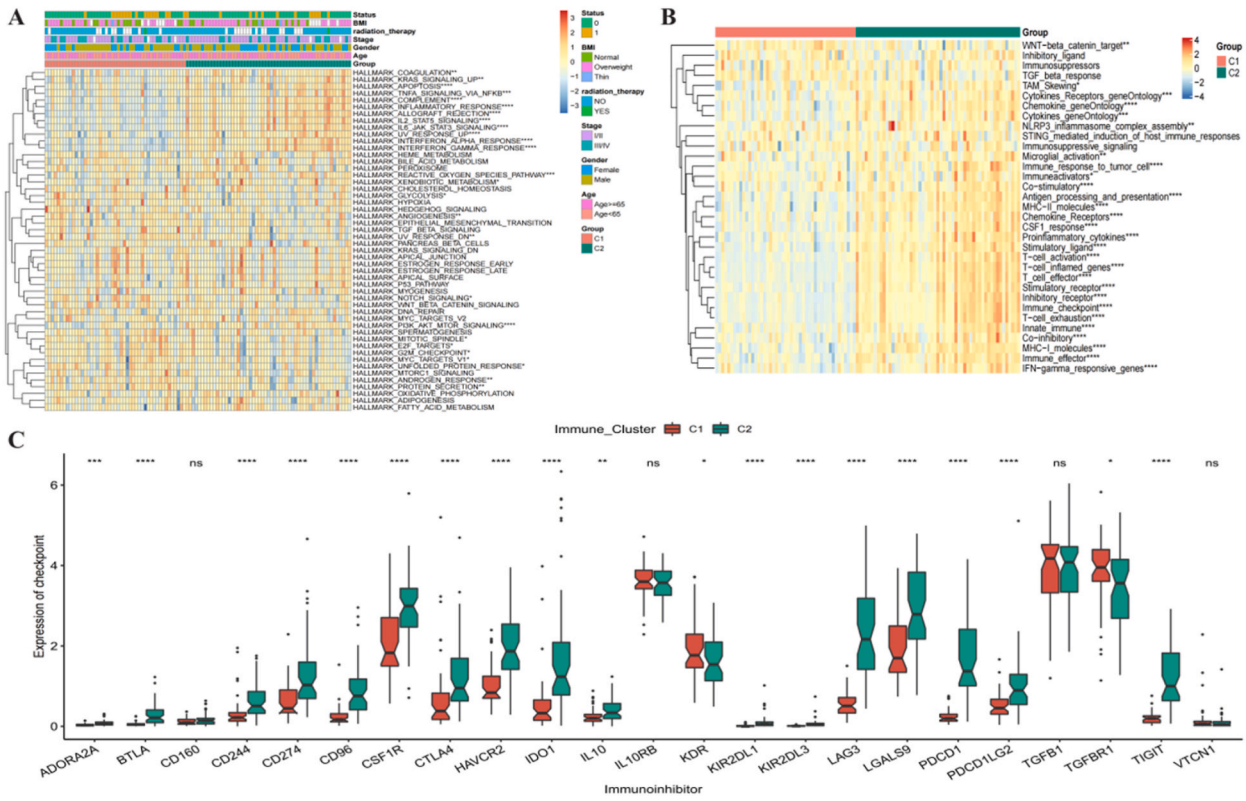

Fig. 6. Functional enrichment differences and expression differences among the immune subtypes. A. Heatmap of the Hallmark pathway enrichment scores among the subtypes; B. Heatmap of the enrichment scores of the special immune function gene sets; C. Differences in the expression of immune checkpoint inhibitors, with red representing C1 and green representing C2. (For interpretation of the references to color in this figure legend, the reader is referred to the Web version of this article.)

related to the prognosis of melanoma were detected (Table S4). Subsequently, 7/10 of TCGA_SKCM set (n = 102) was selected as the training set (n = 71) by random sampling. The lasso linear regression method was used to remove redundant genes in the training set, seed = 2210 was set, and 6 gene signatures were ultimately screened out (Table S5). The results are shown in Fig. 9A–C. The cutoff value was set as the median expression of each gene of the two groups, and the KM survival curves in the overall TCGA set were obtained. The results exhibited considerable variation in the KM curves of the four genes. Among these, the high expression of peroxidasin (*PXDN*) and 3 "-adenosine-5" -phosphosulfate synthase 2 (*PAPSS2*) were risk factors for SKCM (Fig. 9D).

2.4.2. Efficiency of TCGA internal validation model

To further examine the impact of the scores of the six gene signatures on the training set concerning its overall survival, the critical value was considered to be the median of RiskScore, the samples were categorized into high-risk and low-risk groups, and the KM curve was constructed. The analyses revealed a worse prognosis for the high-risk group samples than the low-risk group samples; there was considerable variation in the two groups related to prognosis (Fig. 10A). The constructed receiver operating characteristic (ROC) curve of the prognosis signature was based on the fabricated risk model and the 1 -, 2 -, and 3-year area under the ROC curve (AUC) values were 0.858, 0.982, and 0.937, respectively. This implied that the model score had good predictive efficiency (Fig. 10B). Meanwhile, the scatter plots of survival state and survival time (Fig. 10C) as well as the sample risk score (Fig. 10D) were drawn. The combination of the two scatter plots demonstrated the survival-score link. The training set was examined for the expression of model genes in the two groups (Fig. 10E).

Subsequently, the whole set of TCGA SKCM was used to test the overall survival prediction power of the RiskScore. As per the same method of TCGA training set, the samples were grouped into two risk groups (Supplement Fig. 1A). A considerable variation in the prognosis of the groups could be detected, with a worse prognosis associated with the high-risk group compared to the low-risk group. In TCGA test set, the AUC of 1, 2, and 3 years were 0.770, 0.806, and 0.754, respectively (Supplement Fig. 1B). The scatter plot of the risk score of the overall centralized sample and the scatter plot of the survival time and state were depicted (Supplement Fig. 1C and 1D, respectively). The expression heatmap of the model genes in the overall dataset was examined (Supplement Fig. 1E). A stable and good performance concerning the survival prediction of the model was validated through the results of TCGA overall dataset.

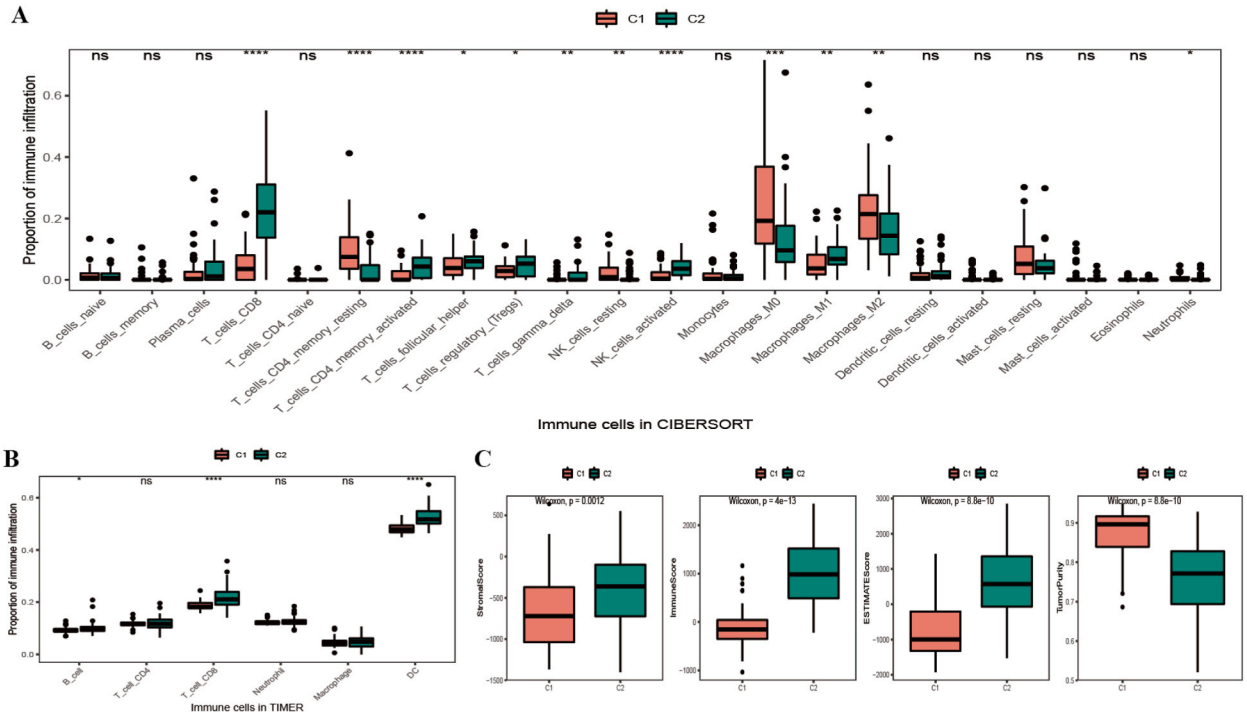

Fig. 7. Functional differences and immune infiltration differences of TCGA immune subtypes. A. Box plots of the difference in the proportion of immune infiltrating cells calculated by the CIBERSORT algorithm, with red representing C1 and green representing C2; B. Box plot of the difference in infiltration ratio of immune cells between subtypes estimated by TIMER algorithm, with red representing C1 and green representing C2; C. Box plots of the differences in the stromal score, immune score, ESTIMATE score, and tumor purity, with red representing C1 and green representing C2. (For interpretation of the references to color in this figure legend, the reader is referred to the Web version of this article.)

2.4.3. Validation of robustness of the model based on external datasets

The capability of the prediction power of the model score was further validated in terms of the overall survival of melanoma patients. The selected GEO external datasets were utilized in this research to conduct the same verification and analysis. The results indicated considerable variation in the two risk groups concerning their prognosis, with a worse prognosis associated with the high-risk group (Supplement Fig. 2A). The respective 1 -, 3 -, and 5-year AUC values were 0.716, 0.731, and 0.647 (Supplement Fig. 2B), indicating efficient predictive efficacy associated with the model score. Meanwhile, the scatter plot of survival time and status (Supplement Fig. 2C) and sample risk score (Supplement Fig. 2D) were derived. The two combined scatter plots facilitated the examination of the survival-score link. The expression of the model genes in the two risk groups was examined (Supplement Fig. 2E).

2.5. Correlation between the risk model and multiple characteristics of the tumors

2.5.1. Risk models were correlated with the clinical features of melanoma

To verify the usage of the risk score as an independent prognostic factor, a univariate cox regression analysis was performed combining the age, sex, and clinicopathological stage of melanoma patients. In the univariate Cox regression analysis, the prognostic model group and stage significantly differed from the reference in the presence of other clinical features (Fig. 11A), proving it to be an independent prognostic factor. Additionally, as per the survival time and status, the nomogram was drawn by combining the clinical indicators of age, gender, and clinicopathological stage (Fig. 11B). The risk score was a clinical factor with a great contribution. The risk score distribution differences among the immune subtypes were examined, wherein the C1 group had considerably enhanced scores than the C2 group; this was consistent with the difference in prognosis in the high-risk group (Fig. 11C).

2.5.2. Differences in the immune microenvironment between the model groups

The variation in the immune microenvironment of the tumor between the two risk groups was examined by comparing the percentage of immune infiltrating cells as per the results of the subtype immune infiltration analysis. The infiltration percentage of the immune cells (22 types) estimated by the CIBERSORT algorithm was examined (Fig. 12A), wherein the percentage of infiltration of 10 of the immune cells varied considerably in the 2 risk groups. A heatmap for the correlation between the model gene expression and the proportion of infiltrating immune-associated cells was constructed (Fig. 12B). The scores of the low-risk group concerning the matrix, immune, and ESTIMATE scores were higher in comparison with the high-risk group and vice versa in terms of tumor purity (Fig. 12C). The box plot of the difference in the proportion of immune infiltration by the TIMER algorithm between the low-risk and high-risk

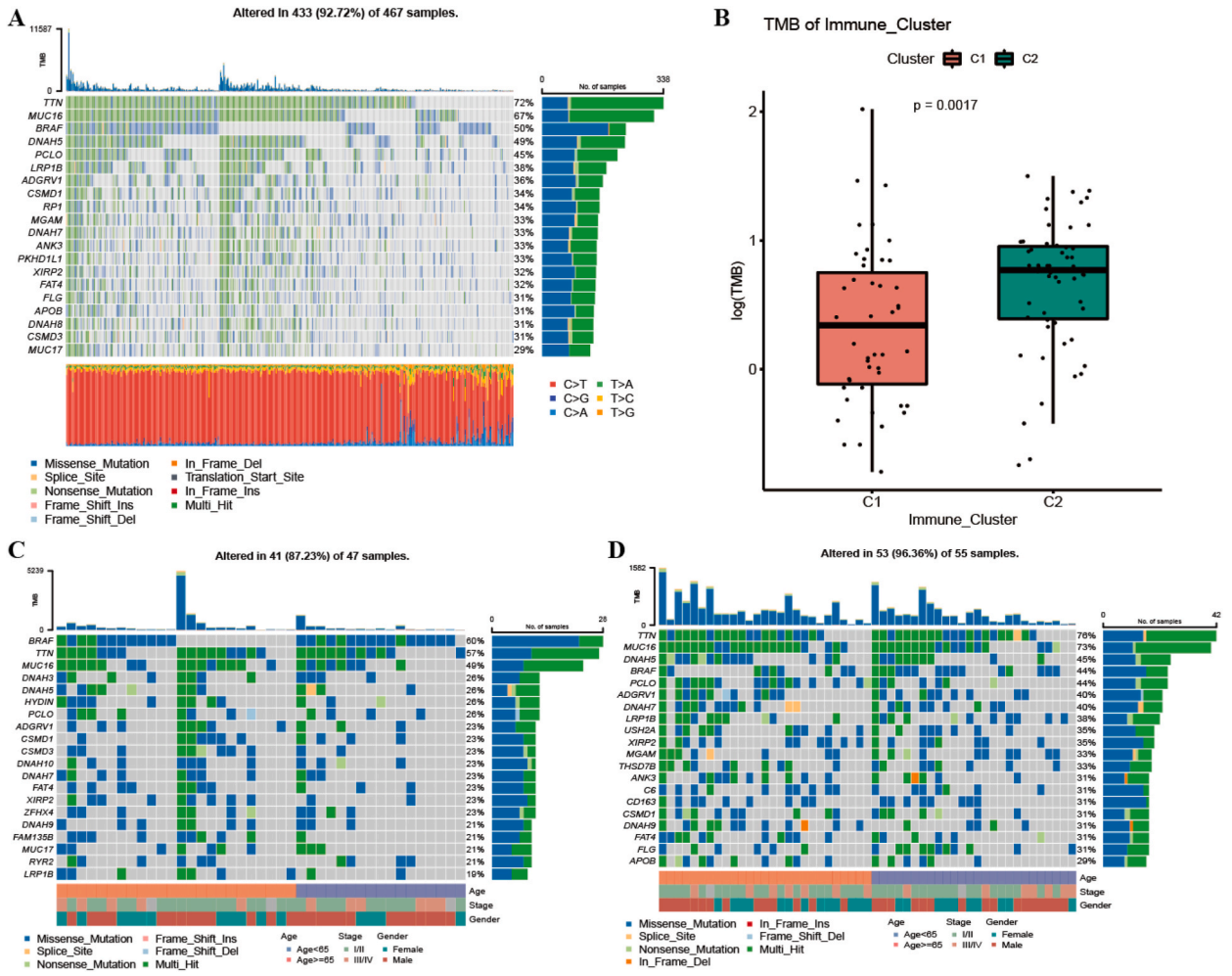

Fig. 8. The SNV differences among TCGA immune subtypes. A. SNV waterfall plot of the TOP20 (mutation frequency) genes in TCGA_SKCM dataset; B. Box plots of the TMB differences between the immune subtypes, with red representing C1 and green representing C2; C. The SNV waterfall map of the TOP20 (mutation frequency) genes in subtype C1; D. The SNV waterfall map of the TOP20 (mutation frequency) genes in subtype C2. (For interpretation of the references to color in this figure legend, the reader is referred to the Web version of this article.)

groups demonstrated a lower proportion of immune infiltrating cells in the former as compared to the latter (Fig. 12D).

2.5.3. *Expression of the immune checkpoints correlated with the model*

Further examination of the correlation between the expression of 23 immune checkpoint inhibitors from the TISIDB database (Table S6) and the expression of 6 model genes, such as the *PXDN* and *PAPSS2*, revealed a weak link with the expression of the immune checkpoints (Supplement Fig. 3A). Box plots were drawn to show the variation in the immune checkpoint expression among the various types of groups. Among the 23 immune checkpoints, 19 genes showed considerable variation in expression, and the expression level was generally lower in the high-risk group (Supplement Fig. 3B).

2.5.4. *Risk model and melanoma genomic mutations*

Gene mutations can promote and lead to the occurrence of cancer or coordinate to drive the malignant growth of cancer. The study of genome-level mutations is crucial for the research and advancement of tumor-targeted drugs and new cancer therapies. The somatic variation distribution among the high-risk and low-risk groups as well as the gene mutation distribution in the samples with different clinical characteristics was depicted through the selection of the frequently mutating top 20 genes in the risk groups to draw a waterfall diagram (Fig. 13A and B, respectively). Compared to the low-risk group, the high-risk group depicted increased mutation frequency of the BRAF gene. Subsequently, the correlation scatter plot for the risk scores and TMB was drawn. The result showed that they were negatively correlated, with a correlation coefficient of 0.31 (Fig. 13C). The division of the samples into high-TMB and low-TMB groups was executed through median grouping, and the KM survival curve was drawn. The former was associated with a better prognosis (Fig. 13D). Finally, a box plot was drawn to show the risk score difference between the two TMB groups. The result indicated an

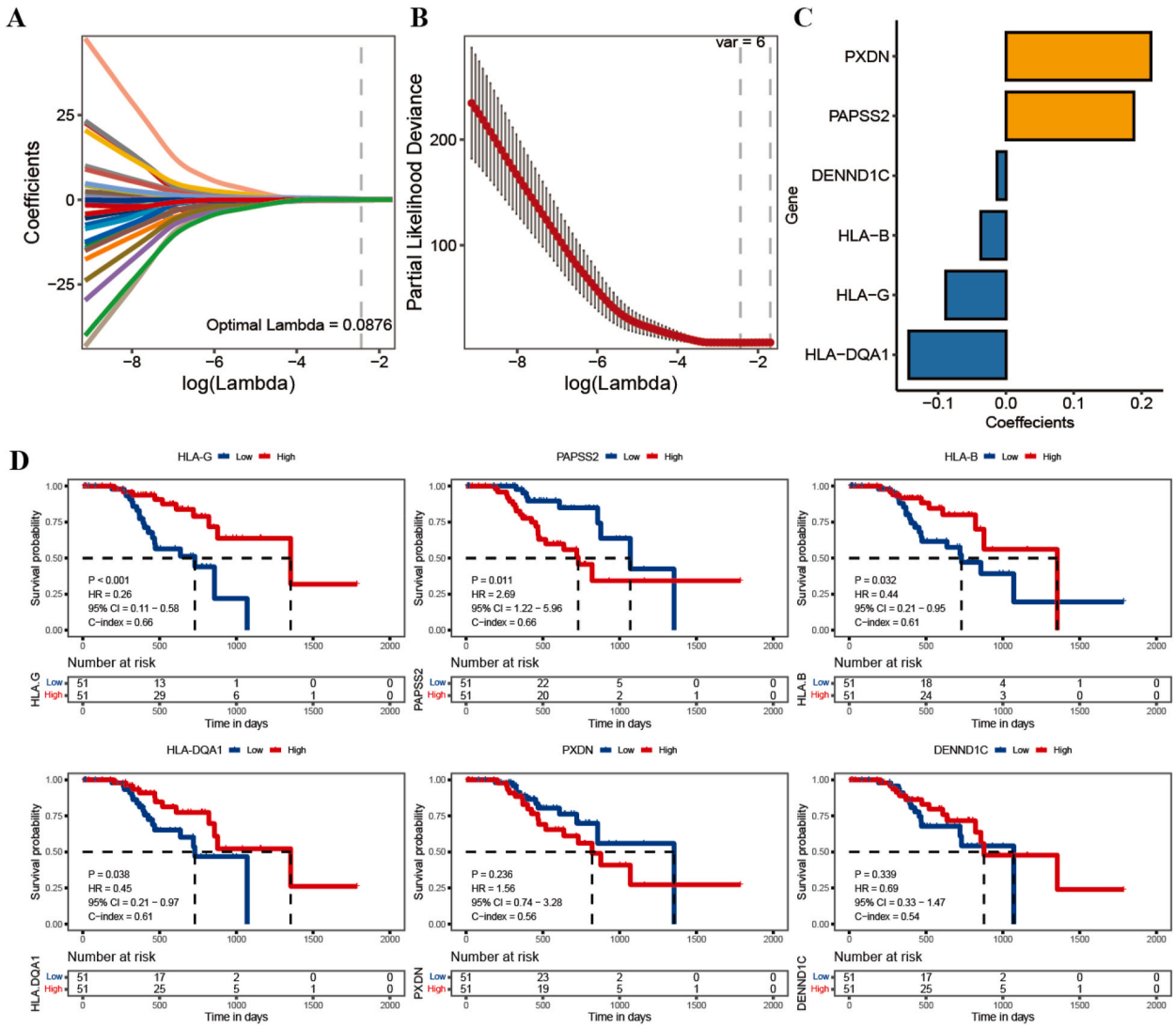

Fig. 9. The Lasso regression analysis results of TCGA dataset. A. The Lasso regression independent variable change trajectory, with abscissa representing the logarithm of the independent variable Lambda and the ordinate representing the coefficient of the independent variable; B. The Lasso regression confidence intervals under each Lambda; C. The Lasso regression coefficients of the key prognostic genes; D. The KM curves of the prognostic signature obtained by the Lasso analysis (with significant differences), with red representing the high-expression group and blue representing the low-expression group. (For interpretation of the references to color in this figure legend, the reader is referred to the Web version of this article.)

increased risk score of the low-TMB group, and there was a considerable variation detected between the two TMB groups (Fig. 13E).

2.5.5. GSVA enrichment analysis

The Hallmark pathway enrichment score of melanoma samples, combined with the model grouping information, was employed to explore the variation in pathway enrichment in the two risk groups. These data were utilized to study the link between the cancer-related characteristic pathways and prognosis. The enrichment scores of 24 pathways were significantly different between the model groups, among which the interferon response factor-related pathways enrichment scores in the low-risk group were higher (Supplement Fig. 4A). Similarly, the sample-based enrichment results of the immuno-specific gene set depicted increased enrichment scores of the low-risk group than those of the high-risk group (Supplement Fig. 4B). This indicated the specific immune functions of the low-risk group. Finally, the link between the model gene expression and the Hallmark pathway enrichment score was quantified. The genes *HLA-B*, *HLA-DQA1*, *HLA-G*, and *DENND1C* were significantly correlated with multiple Hallmark pathways (Supplement Fig. 4C).

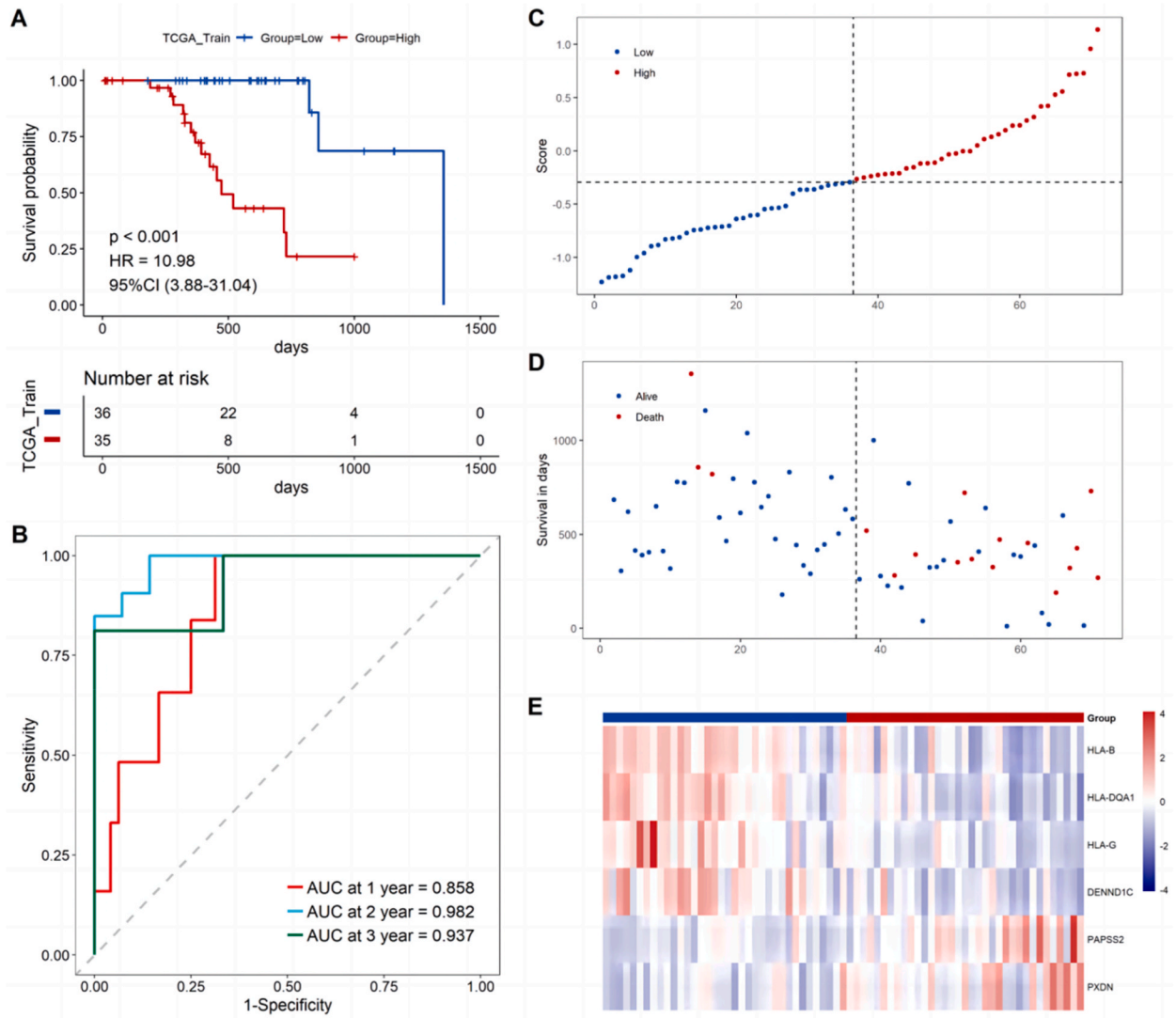

Fig. 10. Prognostic efficacy of TCGA training set validation model. A. The KM curve of TCGA training set; B. The ROC curve; C-E. The risk triplet diagrams, which include the risk distribution point diagram, survival time scatter diagram, and the expression heatmap of model genes in the risk score grouping, with red representing the high-risk group and green representing the low-risk group. (For interpretation of the references to color in this figure legend, the reader is referred to the Web version of this article.)

2.6. Prediction of patient response to treatment by the risk model

2.6.1. Assessment of chemotherapeutic drug resistance by the risk model

Based on TCGA_SKCM expression data, the IC50 values of 138 drugs in the GDSC database were predicted (Table S7). Additionally, the model gene's expression and the IC50 of chemotherapy drugs were subjected to correlation analysis and were investigated (Fig. 14A). According to the model grouping results and the IC50 values, a statistical examination was performed to verify whether there were significant differences in the IC50 values between the two risk groups. Drugs with significant differences were selected to draw an IC50 heatmap (Fig. 14B). A box plot of differences between the two risk groups was also drawn to show the distribution differences of the IC50, wherein four of the drugs were selected for display (Fig. 14C–F). The results of other drugs are shown in the attachment.

2.6.2. Prediction of immunotherapy response by the risk model

The use of model genes as markers of immunotherapy response was detected using IMvigor210. The risk score of each sample was quantified as per the model genes and divided into two risk groups. Furthermore, a KM curve was constructed. The results showed that the survival curves of the risk groups were significantly different, with a worse prognosis associated with the high-risk group (Fig. 15A). The expression distribution of the model genes in the immunotherapy cohort was consistent with that of TCGA and the GEO

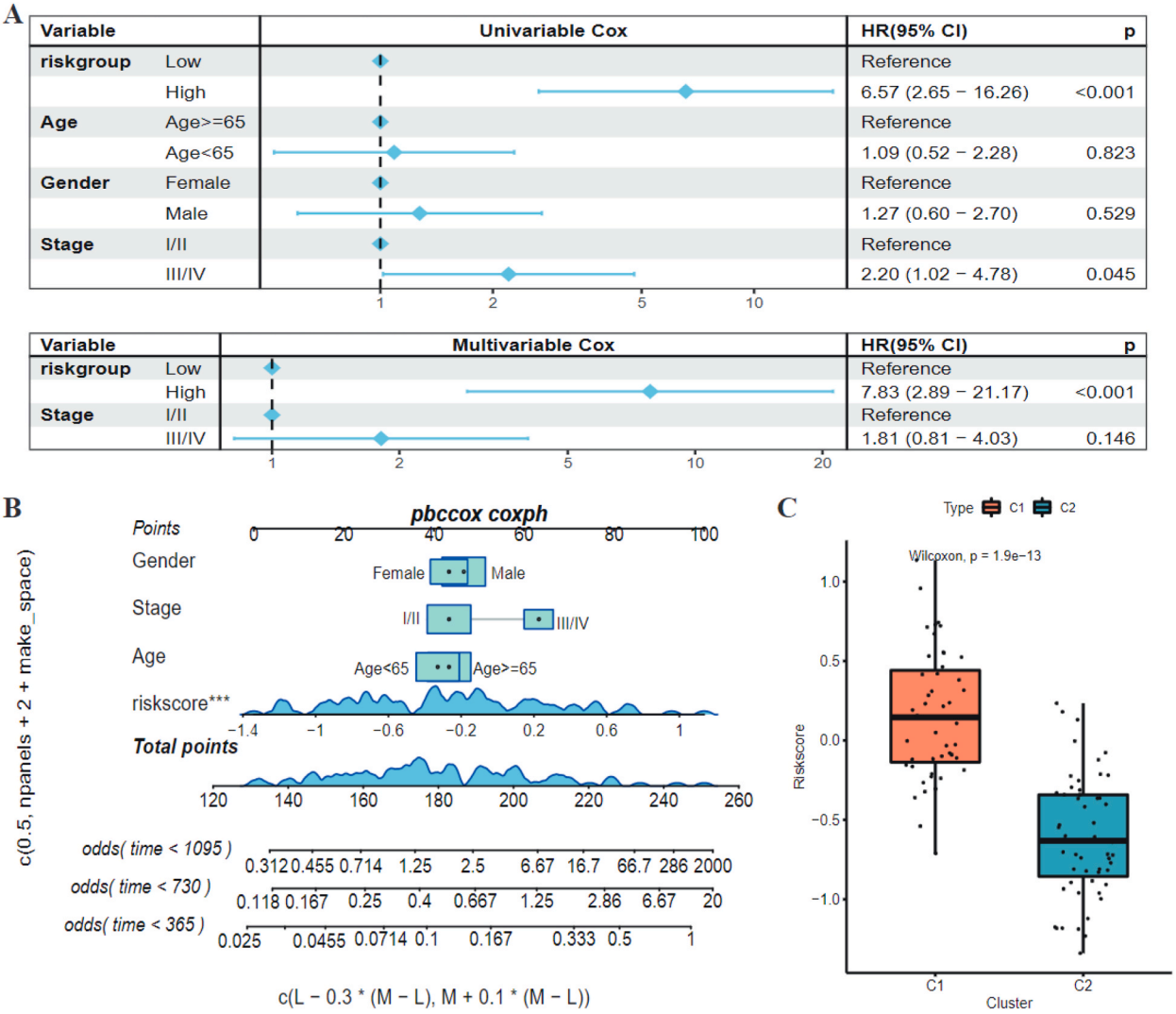

Fig. 11. The independence of the model scores in clinical characteristics. A. The forest map of the univariate Cox analysis results of the clinical factors in TCGA cohort; B. The nomogram of the prediction model. The square plus line segment represents the contribution of the clinical factor to the outcome event. Total Points represent the total score of the single item score after the value of all variables. The bottom three lines represent the survival probability of 3/2/1 year corresponding to each value point; C. Box plot of risk score distribution differences of immune subtype groups, different colors represent different groups, and the P value represents the significant difference. (For interpretation of the references to color in this figure legend, the reader is referred to the Web version of this article.)

cohorts (Fig. 15B). The patients were divided into CR/PR and SD/PD groups as per the immunotherapy response information, and the difference in the model scores in the various response groups was compared. The risk score of the immunotherapy non-response group (PD/SD) was considerably higher than that of the response group (Fig. 15C). Additionally, the cumulative distribution of the immunotherapy response samples differed considerably between the two risk groups (Fig. 15D).

2.7. *PXDN and PAPSS2 act as carcinogens in melanoma*

As shown in Fig. 16A and B, melanoma samples had considerably higher *PXDN* and *PAPSS2* mRNA levels than normal tissues. Furthermore, we transfected the A375 cells. Based on in vitro experiments, we found that silence *PXDN* and *PAPSS2* inhibited the proliferation of melanoma cells (Figs. 17A and 18A). Also increased ROS level (Figs. 17B and 18B) and DNA damage of melanoma cells (Fig. 17C–D and 18C-D, Supplement Fig. 5 and 6). These findings collectively indicated that *PXDN* and *PAPSS2* may act as carcinogens in melanoma.

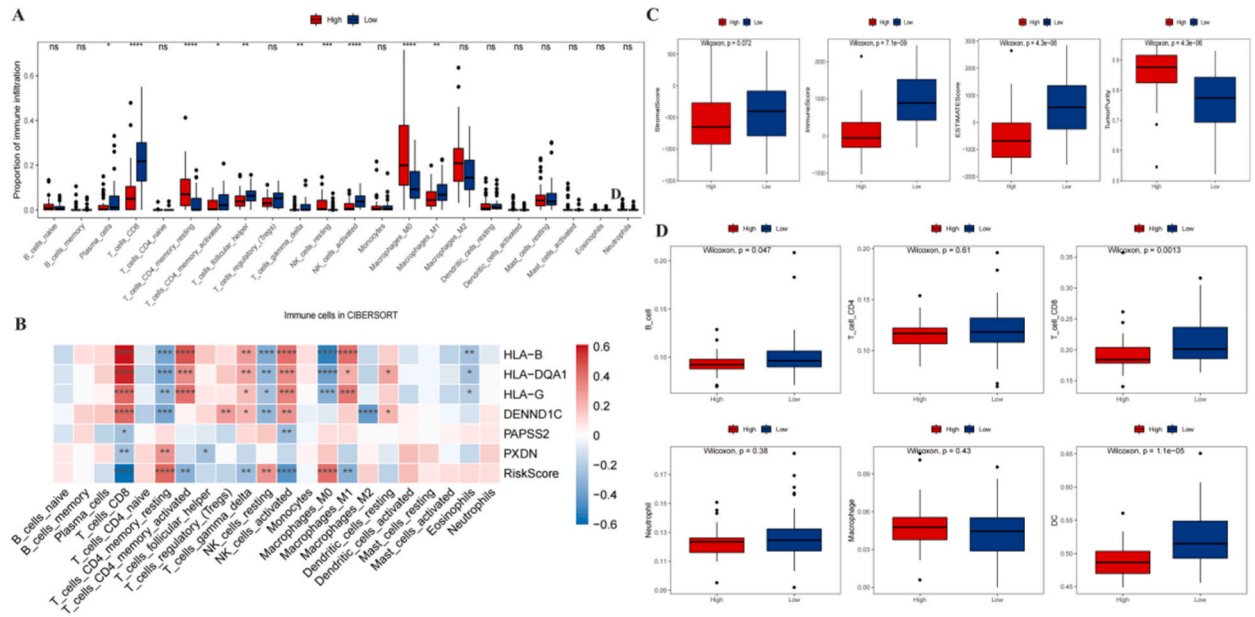

Fig. 12. Differences in the proportion of immune infiltrating cells in the model groups. A. Box plots of the proportion of immune infiltrating cells in the two risk groups according to the CIBERSORT algorithm, with red representing the high-risk group and blue representing the low-risk group; B. Heatmap of the correlation between model genes and the proportion of infiltration of 22 kinds of immune cells estimated by CIBERSORT, with color shade representing the correlation level and * representing the significance; C. Box plots of matrix score, immune score, ESTIMATE score, and tumor purity of the two risk groups, respectively, with red representing the high-risk group and blue representing the low-risk group. D. Box plot of the difference in the infiltration ratio of six immune cell types between the two risk groups estimated by the TIMER algorithm, with red representing the high-risk group and blue representing the low-risk group. (For interpretation of the references to color in this figure legend, the reader is referred to the Web version of this article.)

3. Discussion

In this study, the R package Seurat was initially employed to regroup the malignant tumor cell population in the single-cell dataset to obtain six tumor subsets and the marker genes corresponding to each cell subset. According to the functional identification of each subpopulation of the marker genes, a malignant tumor cell population with immune specificity (C4 subpopulation) was finally identified. Based on the cluster analysis of 62 specific marker genes in the C4 subgroup, TCGA_SKCM patients were divided into 2 immune subtypes, and the prognosis of C2 was significantly better than C1. To clarify the reasons for the difference in prognosis, the differentially-expressed genes among subtypes were further examined, and functional analysis was conducted. The results showed that the aforementioned genes were primarily enriched in the associated molecular pathways of the T-cell and MHC. Prior experiments have indicated that the expression of the MHC molecules determines the strength of cellular immunity, and their expression on the surface of the tumor cells can promote immune cells to recognize tumor antigens [17,18]. T-cells are vital lymphocytes in tumor immunity because they not only serve as “immune watchdogs” for the body, but they may also boost the tumor immune function by directly eradicating the tumor cells and taking the lead in the development of tumor immunity [19]. Therefore, it would not be wrong to hypothesize that the C2 subtype may render the immune function by affecting both the antigen presentation and tumor killing, leading to a better prognosis. Further examination of the immune microenvironment variation among the subtypes revealed a considerably increased expression of immune-related gene sets and immunosuppressive checkpoints in subtype C2 compared to subtype C1. Immune checkpoint inhibitors are the current treatment of choice for patients with advanced or metastatic cutaneous melanoma [20]. Some studies have shown that immune gene pairs can be used for the prediction of the clinical response and prognosis of melanoma patients [21]. Our results suggested that C2 subtype patients are more prone to benefit from immune checkpoint inhibitors. As a novel marker, TMB is strongly linked to the efficacy of immunotherapy for melanoma [22]. Previous studies have shown that among melanoma patients, those with increased TMB have a better prognosis [23]. The number of tumor mutations in the TMB-H was increased. The peptides encoded by these abnormal genes in the tumor cells can be processed and presented by the MHC on the cell surface to form neoplastic antigens. These antigens are recognizable by the body’s T-cells, thereby improving the therapeutic sensitivity of the immune checkpoint inhibitors and affecting patient prognosis [24,25]. The TMB difference between the C1 and C2 subtypes was measured. The analysis indicated that the TMB value of the C2 subtype was higher. Combined with the aforementioned results, the C2 subtype had a better prognosis, which conformed with the conclusions of prior research. Further exploration of the genomic mutations among the immune subtypes revealed a significant increase in the frequency of BRAF mutations in the C1 subtypes with poor prognosis. Studies have shown that about 50% of individuals with melanoma have BRAF mutations, and the most common one is the BRAFV600E mutation [26]. For melanoma patients with BRAF mutation, combination therapy with BRAF inhibitors and

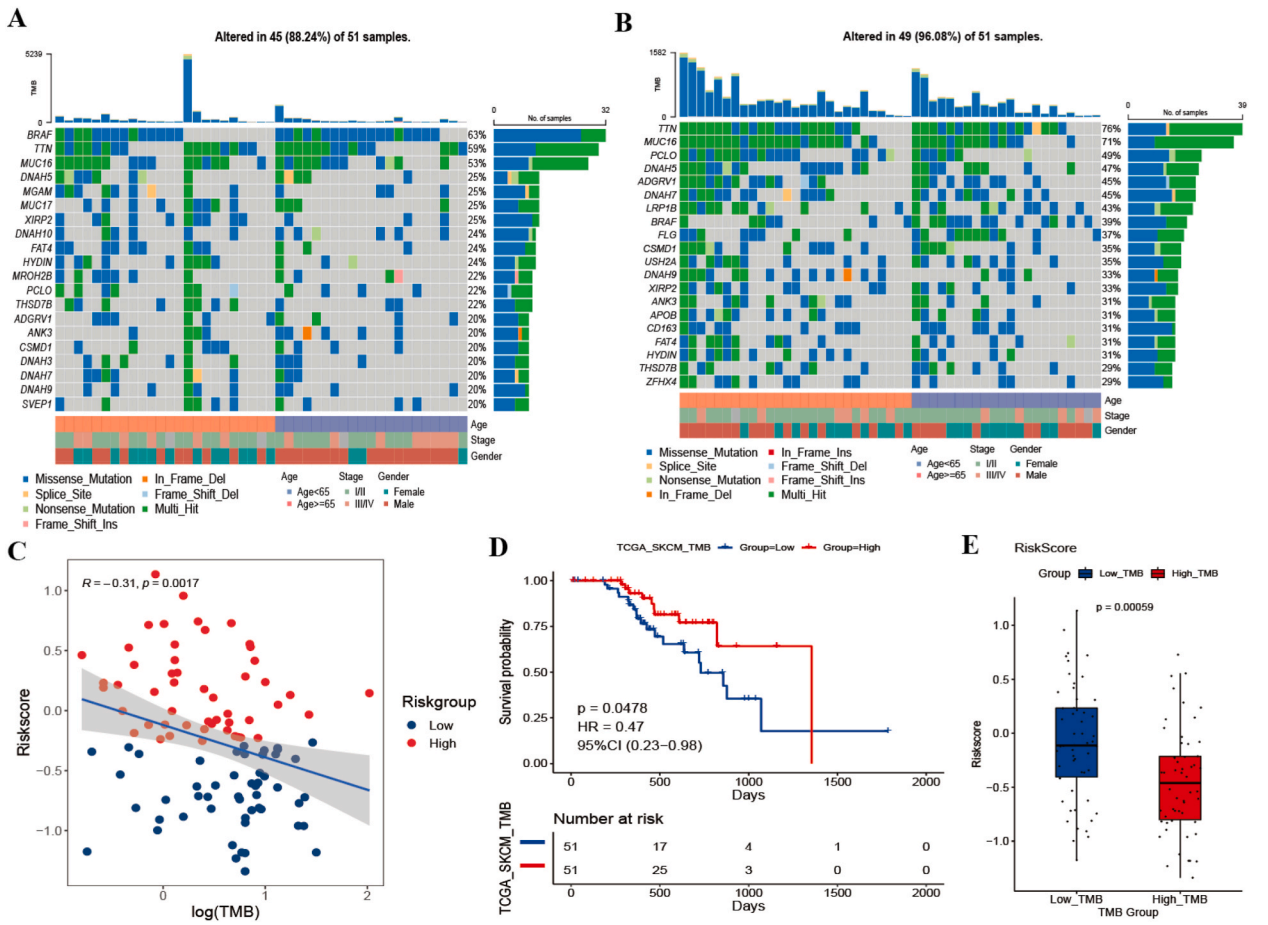

Fig. 13. Mutation differences between the model groups. A-B. The SNV waterfall map of the TOP20 (mutation frequency) genes in the high and low-risk groups; C. The scatter plot of correlation between the risk score and the TMB, with red representing the high-risk group and blue representing the low-risk group; D. The KM curve of the survival difference between the high-TMB and low-TMB groups, with red representing the former and blue representing the latter; E. Box plot of the RiskScore distribution differences between the high-TMB and low-TMB groups, with red representing the former and blue representing the latter. The P value represents a significant difference. (For interpretation of the references to color in this figure legend, the reader is referred to the Web version of this article.)

mitogen-activated extracellular signal-regulated kinase (MEK) inhibitors can significantly improve the prognosis [27]. In conclusion, based on our findings, we recommend BRAF inhibitors for patients with subtype C1 and immune checkpoint inhibitors for patients with subtype C2. Our immunotyping presents a novel strategy for the clinical diagnosis and treatment of melanoma patients.

Furthermore, the genes depicting differential expression among the subtypes were filtered. Ultimately, six prognostic signatures were screened, including *PXDN*, *PAPSS2*, *DENND1C*, *HLA-B*, *HLA-G*, and *HLA-DQA1*. Among these, low expression of *DENND1C*, *HLA-B*, *HLA-G*, and *HLA-DQA1* is associated with poor prognosis of SKCM, the high expression of *PXDN* and *PAPSS2* was linked with a poor prognosis of SKCM. *DENND1C*, *HLA-B*, *HLA-G*, and *HLA-DQA1* have been verified in previous studies, and we will not elaborate here [28–31]. *PXDN* is a heme-containing peroxidase situated in the extracellular matrix and involved in the formation of the extracellular matrix [32]. Studies have reported that *PXDN* may contribute to the process of epithelial-mesenchymal transition and may play a vital role in the formation of tumors [33,34]. The expression of *PXDN* is increased in the malignant progression of melanoma and is involved in its malignant progression [35,36]. In oral squamous cell carcinoma, *PXDN* promotes tumor progression through the Warburg effect [37]. *PAPSS2* is an enzyme that catalyzes the synthesis of active sulfate donor, PAPS, *in vivo*, which may participate in the occurrence and development of tumors through complex regulation of cell proliferation, apoptosis, and estrogen metabolism [38]. In uveal melanoma, *PAPSS2* affects tumor progression through the tumor immune microenvironment [39]. However, the mechanism of *PXDN* and *PAPSS2* in melanoma has not been thoroughly studied. Based on in vitro experiments, we found that ROS levels of melanoma A375 cells increased after transfected si-*PXDN* and si-*PAPSS2*. And melanoma samples had considerably higher *PXDN* and *PAPSS2* mRNA levels than normal tissues. These findings collectively indicated that *PXDN* and *PAPSS2* may act as carcinogens in melanoma. In summary, *PXDN* and *PAPSS2* may regulate the progression of melanoma through the actions of oxidative stress and the tumor immune microenvironment (Fig. 19).

The risk model was developed based on six genes, and the risk model was robust in both the internal and external datasets. As per

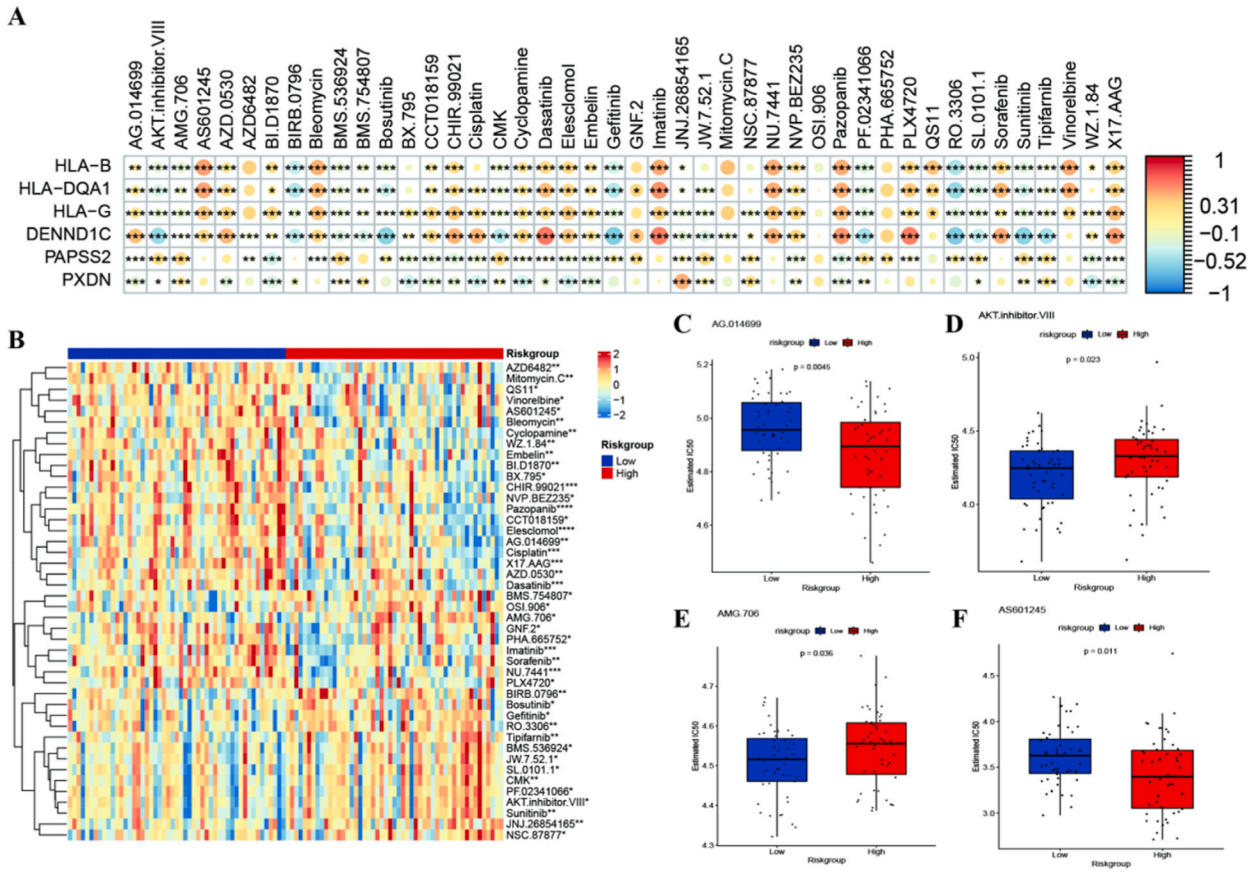

Fig. 14. Prediction of chemotherapeutic drug resistance by the risk model. A. Heatmap of the correlation between the expression of model genes and the IC50 value of drugs, with the color of dots representing the correlation level and * representing the significant differences; B. The IC50 heatmap of significantly different drugs; C-f: Distribution difference of IC50 value of the four randomly-selected chemotherapy drugs between the high-risk and low-risk groups, with red representing the former and blue representing the latter. (For interpretation of the references to color in this figure legend, the reader is referred to the Web version of this article.)

the median risk score, the samples were divided into high-risk and low-risk groups. Differences in the clinical characteristics, immune microenvironment, and gene mutations between the two risk groups were evaluated. The tumor microenvironment includes immune, stromal, and tumor cells as well as the extracellular matrix and other components [40]. Stromal cells can promote and maintain the incidence and progression of tumors, and the infiltration levels of different immune cells are strongly linked to the prognosis of tumors [41]. Therefore, the immune microenvironment variations between the two risk groups were further evaluated using three algorithms. The low-risk group had a higher matrix score, immune score, and ESTIMATE score compared to the high-risk group, while the opposite was the case in terms of the proportion of tumor purity and immune cell infiltration. This indicated that the difference in prognosis between these risk groups may be due to the difference in the immune microenvironment. The importance of the clinical application value of risk models evaluated the ability of these models to predict treatment responses in patients necessary. The analyses indicated that it was much more probable for patients with low-risk scores to benefit from immunotherapy.

This study has some limitations. First is the small sample size of the TCGA_SKCM dataset. Additionally, it was mostly drawn from Western countries. It is essential to expand the sample size and include sequencing results from Asian populations to enhance the predictive ability of the model. Second, this is a retrospective study. A prospective cohort should be designed in the future to further verify the model's accuracy. Finally, the mechanism by which the six genes in the model are involved in the progression of melanoma needs further investigation. Furthermore, as there is currently no evidence of *in vivo* experiments for *PXDN* and *PAPSS2* in melanoma, it would be valuable to conduct animal studies or clinical trials in future research to support the results of this study.

In this study, a population of immunospecific malignant tumor cells was identified based on the single-cell dataset, and TCGA_SKCM cohort of bulk RNA was immunotyped by the specific marker gene of this subpopulation. The prognostic risk model, as per the differentially expressed genes of immunotyping, can be used as a marker of immune response in melanoma patients to guide clinical diagnosis and treatment. Such as targeted therapies or immunotherapeutic approaches, would provide valuable information for clinicians and researchers interested in melanoma treatment strategies.

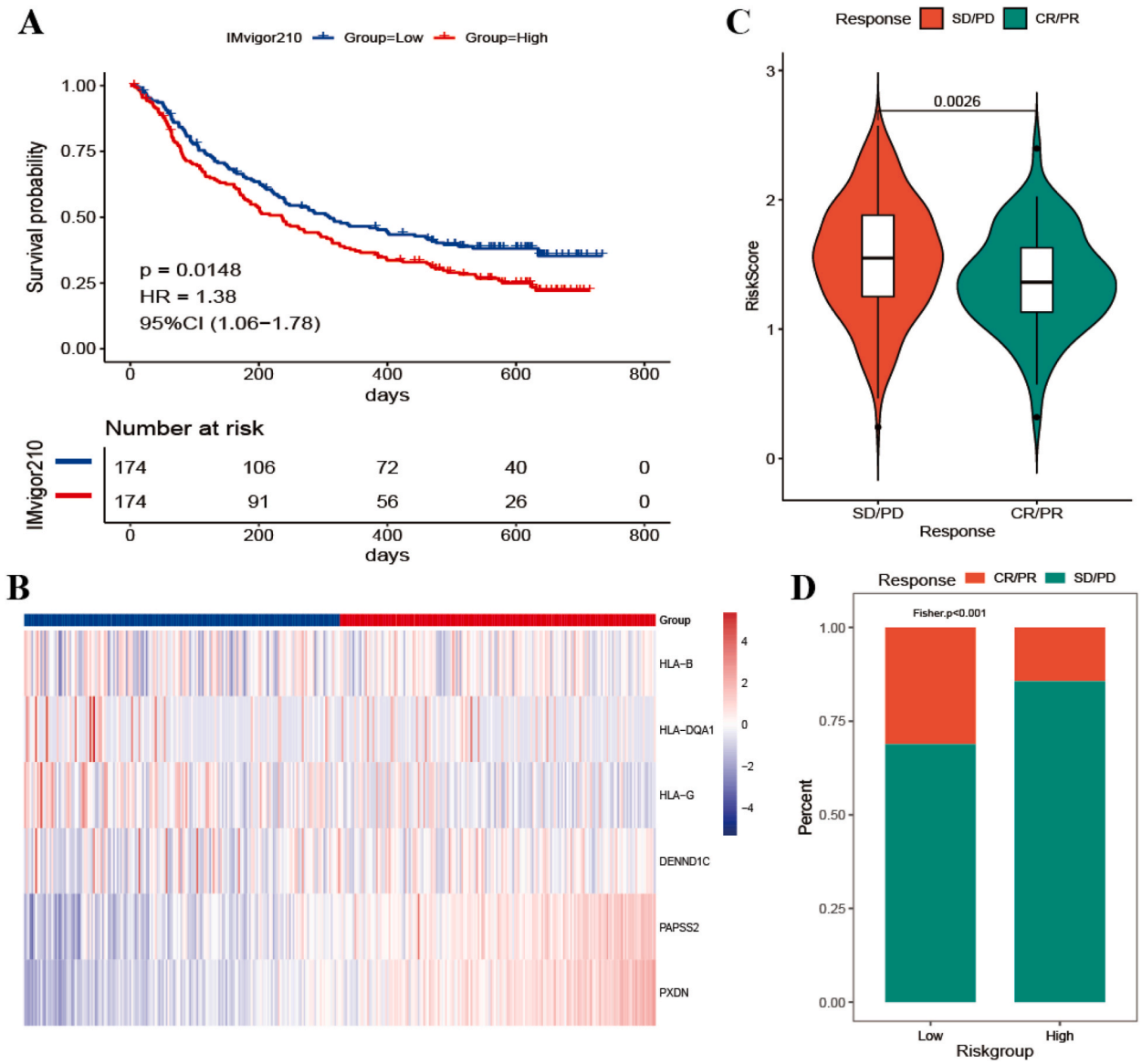

Fig. 15. Prediction of patient treatment response by the risk model. A. The KM curves of the immunotherapy cohort; B. Heatmap of the model gene expression; C. Box plots of risk score distribution for the different immunotherapy response groups; D. Histogram of the cumulative distribution of immunotherapy responses between the high-risk and low-risk groups.

4. Materials and methods

4.1. Data download and preprocessing

The expression matrix and meta information file of the GSE72056 dataset were accessed using the Gene Expression Omnibus (GEO) database (https://www.ncbi.nlm.nih.gov/geo/) as an input file for building the single-cell Seurat. The expression profile and survival information of the GSE65904 were downloaded and processed in the following manner. First, samples with missing clinical follow-up data were excluded. Second, the samples whose survival duration was unknown, was less than 0, or indicated no survival state were removed. "Day" was considered the survival time unit. Third, the probe was converted into a gene symbol. Fourth, the multiple-gene-associated probe was removed. Fifth, the median value was set as the expression of multiple gene symbols. The fragments per kilobase of exon per million mapped fragments (FPKM) expression profile data of the SKCM was accessed at TCGA through the R package TCGAbiolinks, and the log2(FPKM+1) transformation was performed. The corrected TCGA survival information based on already published studies [8] was used for the survival analysis. The genome variations were examined through a detailed analysis of the mutation data. The expression information and clinical annotation information of the urothelial carcinoma dataset IMvigor210 were

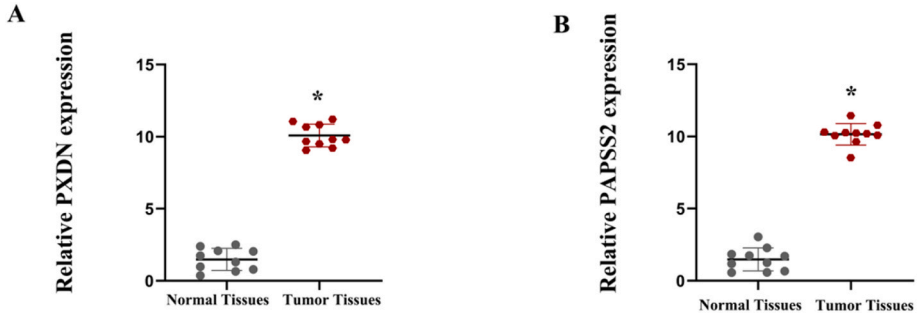

Fig. 16. The mRNA levels of *PXDN* and *PAPSS2*. A. *PDXN* is expressed at high levels in melanoma samples; B. *PAPSS2* is expressed at high levels in melanoma samples; C. ROS levels of melanoma A375 cells increased after transfected si-*PXDN*; D. ROS levels of melanoma A375 cells increased after transfected si-*PAPSS2*.

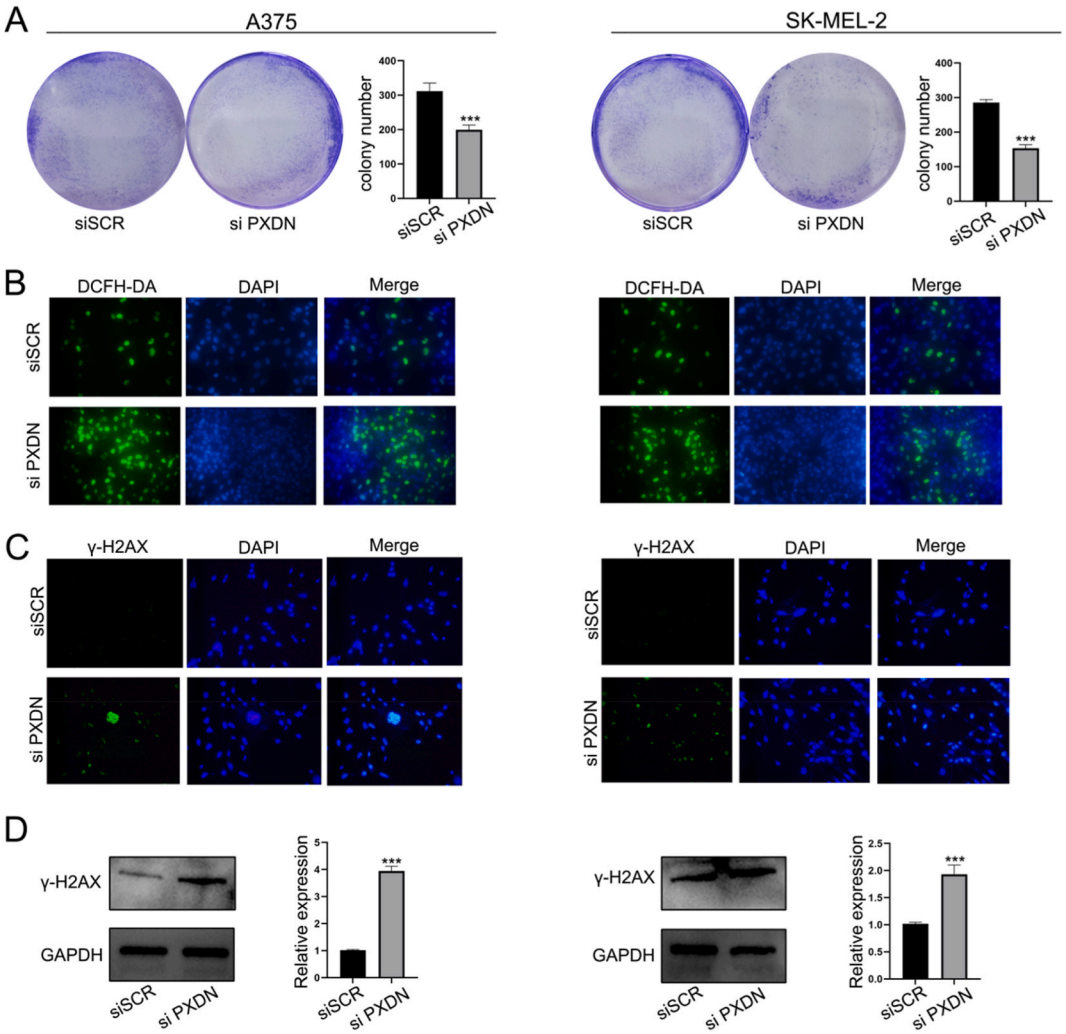

Fig. 17. Effect of *PXDN* on the function of melanoma cells. A. Proliferation of melanoma A375 cells and SKMEL2 cells decreased after transfected si-*PXDN;* B. ROS levels of melanoma A375 cells and SKMEL2 cells increased after transfected si-*PXDN*; C-D. DNA damage of melanoma A375 cells and SKMEL2 cells increased after transfected si-*PXDN*.

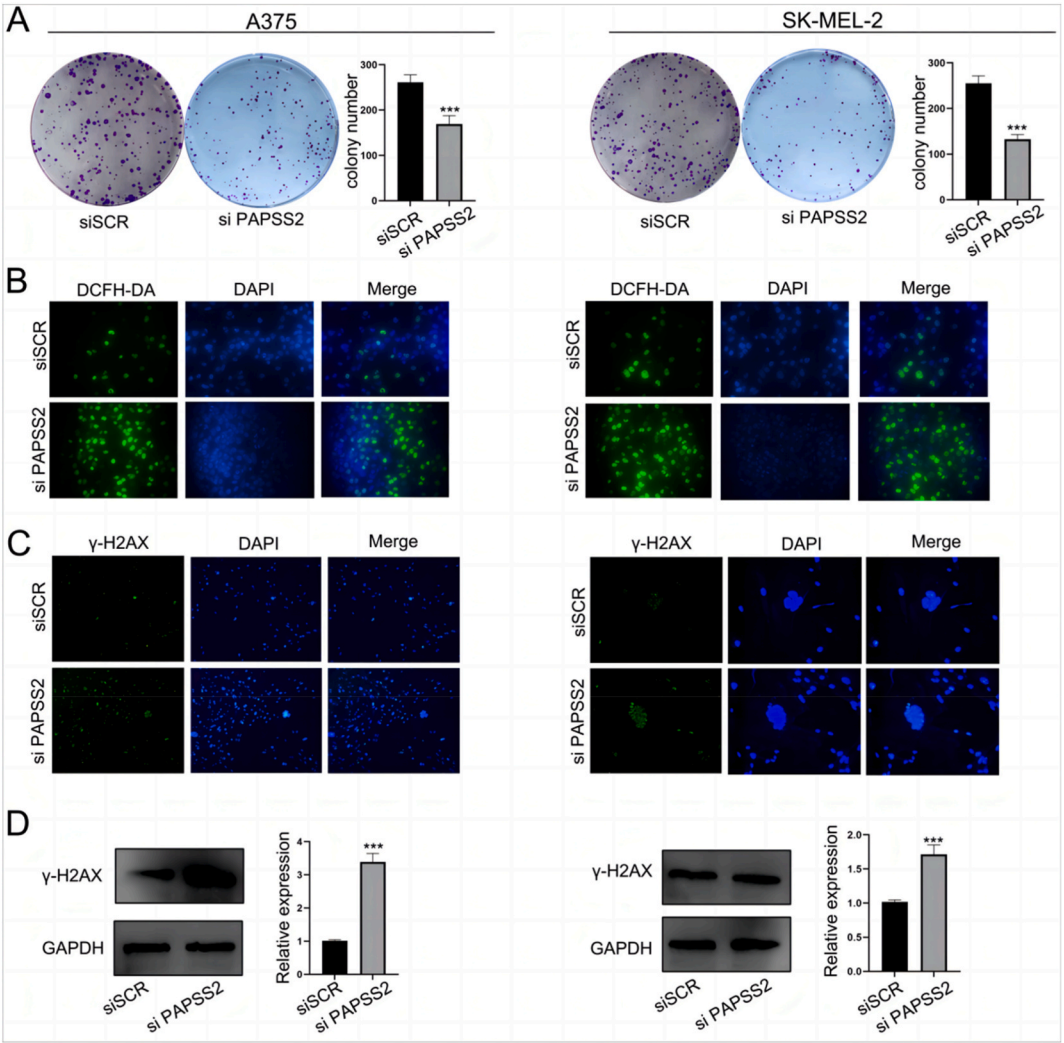

Fig. 18. Effect of *PAPSS2* on the function of melanoma cells. A. Proliferation of melanoma A375 cells and SKMEL2 cells decreased after transfected si-*PAPSS2;* B. ROS levels of melanoma A375 cells and SKMEL2 cells increased after transfected si-*PAPSS2*; C-D. DNA damage of melanoma A375 cells and SKMEL2 cells increased after transfected si-*PAPSS2.*

accessed using IMvigor210 Corebiologies (http://research-pub.gene.com/). The original count was standardized by the R package DEseq2. Subsequently, it was converted to transcripts per million (TPM) values and used as immunotherapy datasets.

4.2. Single-cell data analysis

Single-cell datasets were analyzed using the R package Seurat, a specialized single-cell transcriptome analysis tool. The Seurat object was first built using Seurat's CreateSeuratObject function. The genes and cells were filtered for the first time, with the minimum number of cells set at 3 and the minimum number of features set at 200. The cells were filtered again, with the number of features and cell counts set in a range of 200–6000 and 300 to 40000, respectively; the overexpression doublet_cutoff was set as 0.15. The mitochondrial genes were lower than 30%, and the proportion of red blood cells read lower than 20%. After principal component analysis (PCA), the batch correction was executed using the R package Harmony to prevent the batch effects from interfering with the downstream analysis. Subsequently, according to the ElbowPlot() function, the first 15 PCs were identified as important for subsequent analysis. After debugging, FindClusters was used to identify tumor cell subsets and regroup malignant cells with a resolution of 0.6. The function FindAllMarkers() was utilized to identify the marker genes of subsets with min.pct = 0.25 and logfc.threshold = 0.25. The UMAP is a popular learning technique for dimensionality reduction based on the theoretical framework and geometric generation data. The dimensionality of the data after the PCA was further reduced by the UMAP. The cell types were divided in the low-dimensional space, and the DimPlot function was used for visualization. Finally, the functions FeaturePlot, DotPlot, DoHeatmap, and VlnPlot were used to visualize the landscape of tumor cells and the expression distribution of the characteristic genes. When using DotPlot to

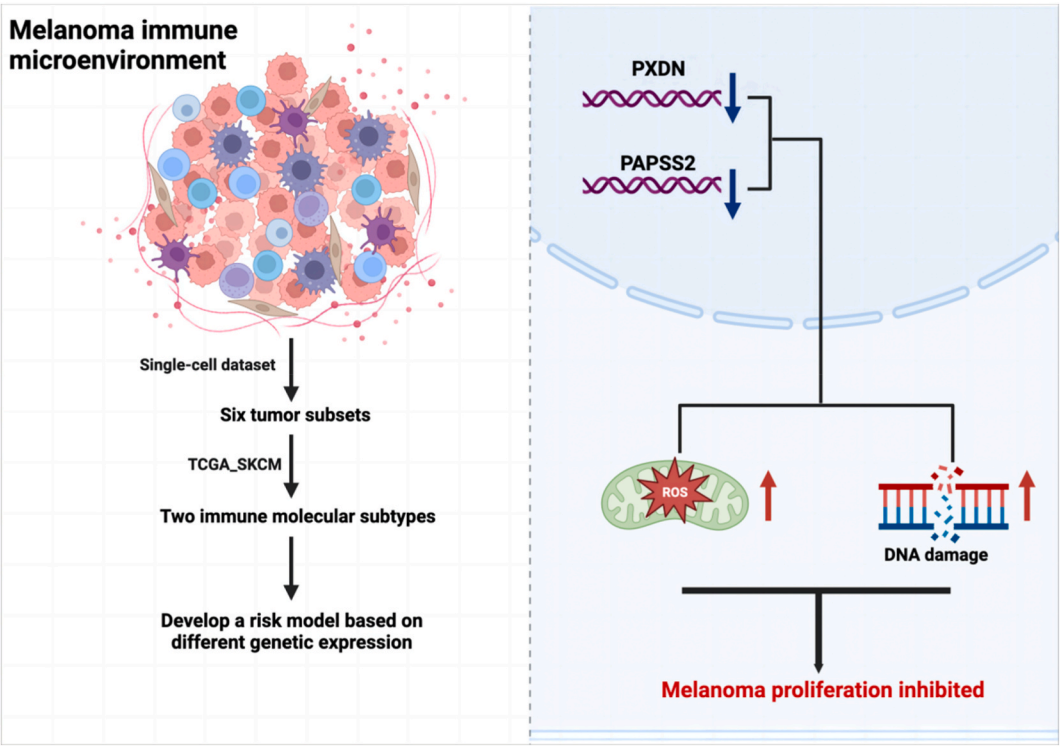

Fig. 19. Mechanism for the regulatory function of *PXDN* and *PAPSS2* in melanoma progression.

visualize specific marker genes in cell subsets, the threshold was set at avg_log2FC $>$ 0.585.

4.3. Cell communication

CellChat is an R package for inferring cell-to-cell communication as per the scRNA-seq [9]. CellChatDB contains well-supported interactions of ligands with receptors concerning mice and humans, including polymer and coenzyme factors. CellChatDB.human, in turn, contains various ligand libraries, which can be used to elaborate the relationship between cells from a specific perspective. For this analysis, all CellChatDB.human Secreted Signaling was employed to infer the cell-to-cell communication present in the single-cell data.

4.4. Enrichment analysis

The R package ClusterProfiler [10] was employed for performing the gene set enrichment analysis (GSEA) on the characteristic genes of the cell subsets based on the Hallmark and Kyoto Encyclopedia of Genes and Genomes (KEGG) pathway gene sets. $P < 0.05$ was set as the GMT of the significant enrichment. For each sample, the single-sample GSEA (ssGSEA) algorithm of gene set variation analysis (GSVA) in the R package was employed for quantifying the enrichment scores of 50 Hallmark pathways and special immune function gene sets [11] as per the gene expression of TCGA melanoma samples. The statistical tests were then used to calculate the variation in enrichment scores among the groups. The R package heatmap was utilized for drawing an enrichment score heatmap combined with the samples' clinical characteristics.

4.5. Unsupervised clustering analysis

The ConsensusClusterPlus R package was employed for consensus clustering analysis of the SKCM samples to identify the specific immune subtypes. An 80% resampling rate and 1000 replicates were used for ensuring classification stability. Subsequently, the Kaplan-Meier (KM) survival curve was drawn by the R package Survival, while the log-rank test was employed for determining the significance of the prognostic variation between the different types. Finally, the clustering results, with an efficient clustering effect and considerable differences in survival between the subtypes, were selected as the typing results.

4.6. Differential expression analysis

The differential expression concerning the various immune subtypes was analyzed through the R package Limma [12]. The genes

with associated differential expression were filtered out using the Benjamini-Hochberg (FDR)-corrected P value adj.pvalue<0.05 and | log2FC | >0.585 (1.5 times FoldChange value as cutoff) thresholds.

4.7. Survival analysis

The median gene expression level was used as the cutoff point to group the SKCM tumor samples as per their high or low expression. Thereafter, the prognosis analysis was executed using the generated survival curves, and the significance of the differences was calculated. The KM method was utilized for the former, while the latter was performed using the log-rank test. Genes with $P < 0.05$ were identified as the prognostic genes significantly associated with the SKCM prognosis.

4.8. Estimation of the proportion of immune infiltrating cells and the immune score

Based on the expression profile of TCGA_SKCM dataset, CIBERSORT [13], ESTIMATE, and TIMERxCell algorithms of the R package IOBR [14] were utilized for quantifying the infiltrating immune cells.

4.9. Genomic SNV analysis

Based on the mutation annotation format (MAF) file of the somatic mutation detection results of TCGA_SKCM cohort, a waterfall diagram was drawn using the oncoplot function of Maftools [15] to show the SNV mutation differences across the different groups. Each sample's tumor mutation burden (TMB) was calculated to study the relationship between the immune subtypes or model groups and the TMB.

4.10. Drug susceptibility

The selected 138 drugs from the GDSC database were tested for their sensitivity through the R package pRRophetic [16] in combination with the gene expression data from the SKCM cohort (IC50 value). Statistical tests were utilized to check the significance of the IC50 differences in the high-risk and low-risk groups. The drugs with significant differences were selected to draw a heatmap of IC50. Spearman's algorithm was used to calculate the correlation between the IC50 value of the different drugs and the model gene's expression. Additionally, the box plot of the IC50 distribution of both the risk groups was drawn to elucidate the relationship between the model and chemotherapy drugs.

4.11. Tissue samples

Melanoma samples and adjacent non-tumor tissues were collected from 10 patients (all>18 years of age), immediately placed in liquid nitrogen and preserved at −80 °C. None of the patients received any preoperative anti-tumor therapies. All patients and their families were fully informed as to the purpose of the study and informed consent was obtained from all participants. This study was approved by the Ethics Committee of the First Hospital of China Medical University.

4.12. RNA isolation and RT-PCR analysis

RNA extraction from tissues was performed using the TRIzol reagent (Invitrogen, Carlsbad, CA, USA). RNA was reverse-transcribed into cDNA with use of the QuantiTect Reverse Transcription Kit (QIAGEN, Valencia, CA, USA). Real-time PCR analyses were quantified by SYBR-Green (Takara, Otsu, Shiga, Japan) and levels were normalized to GAPDH levels. Sequences of upstream and downstream primers were as follows. *PXDN*: 5′-CAGGGACCTCGTTAATGGCT-3′ and 5′-CCGTTCAGACAGCTGACGTT-3′. *PAPSS2*: 5′-TGGTGCTGGGAAAACAACCA-3′ and 5′-TCCCCCGCAGAGAATCCCAG-3′.

4.13. Cell culture and transfection

A375 cell line and SKMEL2 cell line were obtained from the Chinese Academy of Sciences and were cultured in DMEM supplemented with 10% fetal bovine serum (FBS; Gibco) and 1% penicillin-streptomycin in an incubator with humidified 5% CO_2 at 37 °C. At 24 h before transfection, A375 cells and SKMEL2 cells were planted in six-well plates with 50–60% confluence and then transfected with siRNA by using Lipofectamine 2000 according to the manufacturer's instructions.

4.14. Measurement of intracellular ROS levels and DNA damage

The intracellular ROS levels were measured using a Reactive Oxygen Species Assay Kit (Beyotime Biotechnology, China); 2′, 7′-dichlorofluorescein-diacetate (DCFH-DA), which is easily oxidized to fluorescent dichlorofluorescein (DCF) by intracellular ROS, is its principal component, and therefore, the ROS levels were quantified. Following the treatment, the cells were incubated with DCFH-DA for 20min at 37 °C and then observed using fluorescence microscopy (Nikon) and measured at 488 nm excitation and 525 nm emission by a fluorescence spectrophotometer (BioTek). Similarly, DNA Damage Assay Kit was used to measure DNA damage in cells (Beyotime Biotechnology, China).

4.15. Colony-forming experiments

The scrambled siRNA (siSCR), si-*PXDN*, and si-P*APSS2* were all transfected into cell cultures in 96-well plates. Cells (500/well) treated with siRNAs for colony-forming experiments were added to 12-well plates. The colonies were counted after two weeks.

4.16. Western blot assay

Cells were lysed using RIPA Lysis containing Protease/Phosphatase Inhibitor Cocktail (Abcam). The extracted proteins were separated in 10% SDS-polyacrylamide gel and then transferred to immobilon-P membranes (Merck Millipore). The membrane was blocked with 5% nonfat dry milk in PBS containing 0.1% Tween 20 (PBST) for 1 h at room temperature and then incubated with primary antibodies at 4 °C overnight. The next day, the membranes were washed three times with Tris-buffered saline Tween and then incubated with HRP-conjugated secondary antibody (1:1000, Santa Cruz Biotech) for 2 h at room temperature. Finally, all bands were detected using ECL Western blotting kit (Amersham Biosciences). GAPDH was used as an internal reference.

4.17. Statistic analysis

Variations in the two groups of the samples as well as among the multiple groups were compared. The Wilcoxon test was employed for the former, while the Kruskal−Wallis test was used for the latter, wherein "ns" represented $p > 0.05$, * represented $p \leq 0.05$, ** represented $p \leq 0.01$, *** represented $p \leq 0.001$, and **** represented $p \leq 0.0001$.

Ethics approval and consent to participate

This study was exempted by the institutional ethics committee of the First Hospital of China Medical University (2023-53).

Consent for publication

Not applicable.

Availability of data and materials

The datasets used and/or analyzed during the current study are available from the corresponding author on reasonable request.

Funding

This work was supported by Peking University Shenzhen Hospital Scientific Research Fund KYQD2023300.

CRediT authorship contribution statement

Yaling Li: Writing – original draft, Data curation, Conceptualization. **Bin Jiang:** Project administration, Methodology. **Bancheng Chen:** Project administration. **Yanfen Zou:** Supervision. **Yan Wang:** Project administration. **Qian Liu:** Project administration. **Bing Song:** Writing – review & editing, Project administration. **Bo Yu:** Writing – review & editing, Project administration.

Declaration of competing interest

The authors declare the following financial interests/personal relationships which may be considered as potential competing interests:Yaling Li reports financial support was provided by Peking University Shenzhen Hospital.

Acknowledgments

Not applicable.

Appendix A. Supplementary data

Supplementary data to this article can be found online at https://doi.org/10.1016/j.heliyon.2024.e28244.

References

[1] J.A. Santamaria-Barria, J. Mammen, Surgical Management of melanoma: Advances and Updates, Curr. Oncol. Rep. 24 (11) (2022) 1425–1432.
[2] R.L. Siegel, et al., Cancer Statistics, 2021, Ca - Cancer J. Clin. 71 (1) (2021) 7–33.

[3] C.G. Watts, et al., Clinical features associated with individuals at higher risk of melanoma: a population-based study, JAMA Dermatol 153 (1) (2017) 23–29.
[4] Y. Yan, et al., Understanding heterogeneous tumor microenvironment in metastatic melanoma, PLoS One 14 (6) (2019) e0216485.
[5] T. Baslan, J. Hicks, Unravelling biology and shifting paradigms in cancer with single-cell sequencing, Nat. Rev. Cancer 17 (9) (2017) 557–569.
[6] S.Z. Wu, et al., A single-cell and spatially resolved atlas of human breast cancers, Nat. Genet. 53 (9) (2021) 1334–1347.
[7] A.J. Nirmal, et al., The spatial landscape of progression and Immunoediting in primary melanoma at single-cell resolution, Cancer Discov. 12 (6) (2022) 1518–1541.
[8] J. Liu, et al., An Integrated TCGA pan-cancer clinical data resource to drive high-Quality survival outcome Analytics, Cell 173 (2) (2018) 400–416. .e11.
[9] S. Jin, et al., Inference and analysis of cell-cell communication using CellChat, Nat. Commun. 12 (1) (2021) 1088.
[10] T. Wu, et al., clusterProfiler 4.0: a universal enrichment tool for interpreting omics data, Innovation 2 (3) (2021) 100141.
[11] K. Yang, et al., Identification of a unique tumor cell subset employing myeloid transcriptional circuits to create an immunomodulatory microenvironment in glioblastoma, OncoImmunology 11 (1) (2022) 2030020.
[12] M.E. Ritchie, et al., Limma powers differential expression analyses for RNA-sequencing and microarray studies, Nucleic Acids Res. 43 (7) (2015) e47.
[13] A.M. Newman, et al., Robust enumeration of cell subsets from tissue expression profiles, Nat. Methods 12 (5) (2015) 453–457.
[14] D. Zeng, et al., IOBR: multi-omics immuno-oncology biological research to decode tumor microenvironment and signatures, Front. Immunol. 12 (2021) 687975.
[15] A. Mayakonda, et al., Maftools: efficient and comprehensive analysis of somatic variants in cancer, Genome Res. 28 (11) (2018) 1747–1756.
[16] P. Geeleher, N. Cox, R.S. Huang, pRRophetic: an R package for prediction of clinical chemotherapeutic response from tumor gene expression levels, PLoS One 9 (9) (2014) e107468.
[17] S.S. Gu, et al., Therapeutically increasing MHC-I expression potentiates immune checkpoint blockade, Cancer Discov. 11 (6) (2021) 1524–1541.
[18] D. Dersh, J. Hollý, J.W. Yewdell, A few good peptides: MHC class I-based cancer immunosurveillance and immunoevasion, Nat. Rev. Immunol. 21 (2) (2021) 116–128.
[19] A.D. Waldman, J.M. Fritz, M.J. Lenardo, A guide to cancer immunotherapy: from T cell basic science to clinical practice, Nat. Rev. Immunol. 20 (11) (2020) 651–668.
[20] F. Sabbatino, et al., Immune checkpoint inhibitors for the treatment of melanoma, Expert Opin Biol Ther 22 (5) (2022) 563–576.
[21] J. Yan, et al., An immune-related gene pair index predicts clinical response and survival outcome of immune checkpoint inhibitors in melanoma, Front. Immunol. 13 (2022) 839901.
[22] A.M. Goodman, et al., Tumor mutational burden as an independent predictor of response to immunotherapy in diverse cancers, Mol. Cancer Ther. 16 (11) (2017) 2598–2608.
[23] S. Heeke, et al., In-house implementation of tumor mutational burden testing to predict durable clinical benefit in non-small cell lung cancer and melanoma patients, Cancers 11 (9) (2019).
[24] R. Büttner, et al., Implementing TMB measurement in clinical practice: considerations on assay requirements, ESMO Open 4 (1) (2019) e000442.
[25] L.E. Hendriks, E. Rouleau, B. Besse, Clinical utility of tumor mutational burden in patients with non-small cell lung cancer treated with immunotherapy, Transl. Lung Cancer Res. 7 (6) (2018) 647–660.
[26] L. Gerosa, et al., Receptor-driven ERK pulses reconfigure MAPK signaling and enable persistence of drug-adapted BRAF-mutant melanoma cells, Cell Syst 11 (5) (2020) 478–494. .e9.
[27] M. Doepner, I.Y. Lee, T.W. Ridky, Drug resistant melanoma may Be vulnerable to inhibitors of serine synthesis, J. Invest. Dermatol. 140 (11) (2020) 2114–2116.
[28] Y. Gu, et al., PCSK9 facilitates melanoma pathogenesis via a network regulating tumor immunity, JOURNAL OF EXPERIMENTAL & CLINICAL CANCER RESEARCH 42 (1) (2023) 2.
[29] A. Dhall, et al., Computing skin cutaneous melanoma outcome from the HLA-alleles and clinical characteristics, Front. Genet. 11 (2020) 221.
[30] S. Marletta, et al., HLA-G expression in melanomas, Int. Rev. Immunol. 40 (5) (2021) 330–343.
[31] Z.H. Ji, et al., Identification of immune-related biomarkers associated with tumorigenesis and prognosis in skin cutaneous melanoma, Am. J. Cancer Res. 12 (4) (2022) 1727–1739.
[32] G. Cheng, R. Shi, Mammalian peroxidasin (PXDN): from physiology to pathology, Free Radic. Biol. Med. 182 (2022) 100–107.
[33] Y.Z. Zheng, L. Liang, High expression of PXDN is associated with poor prognosis and promotes proliferation, invasion as well as migration in ovarian cancer, Ann. Diagn. Pathol. 34 (2018) 161–165.
[34] X. Zhou, et al., A systematic pan-cancer analysis of PXDN as a potential target for clinical diagnosis and treatment, Front. Oncol. 12 (2022) 952849.
[35] L. Carvalho, et al., Redox-related proteins in melanoma progression, Antioxidants 11 (3) (2022).
[36] A. Jayachandran, et al., Identifying and targeting determinants of melanoma cellular invasion, Oncotarget 7 (27) (2016) 41186–41202.
[37] M. Kurihara-Shimomura, et al., Peroxidan plays a tumor-promoting role in oral squamous cell carcinoma, Int. J. Mol. Sci. 21 (15) (2020) 5416.
[38] Y. Zhang, et al., Enhanced PAPSS2/VCAN sulfation axis is essential for Snail-mediated breast cancer cell migration and metastasis, Cell Death Differ. 26 (3) (2019) 565–579.
[39] H. Luo, C. Ma, Identification of prognostic genes in uveal melanoma microenvironment, PLoS One 15 (11) (2020) e0242263.
[40] Y. Xiao, D. Yu, Tumor microenvironment as a therapeutic target in cancer, Pharmacol. Ther. 221 (2021) 107753.
[41] M. Jarosz-Biej, et al., Tumor microenvironment as A "game changer" in cancer radiotherapy, Int. J. Mol. Sci. 20 (13) (2019).